

## The *Chandra* Large Area Synoptic X-ray Survey (CLASXS) of the Lockman Hole-Northwest: The X-ray Catalog

Y. Yang<sup>1,2</sup>, R. F. Mushotzky<sup>2</sup>, A. T. Steffen<sup>3</sup>, A. J. Barger<sup>3,4,5</sup>, L. L. Cowie<sup>5</sup>

### ABSTRACT

We present the X-ray catalog and basic results from our *Chandra* Large Area Synoptic X-ray Survey (CLASXS) of the Lockman Hole-Northwest field. Our 9 ACIS-I fields cover a contiguous solid angle of  $\sim 0.4 \text{ deg}^2$  and reach fluxes of  $5 \times 10^{-16} \text{ ergs cm}^{-2} \text{ s}^{-1}$  (0.4–2 keV) and  $3 \times 10^{-15} \text{ ergs cm}^{-2} \text{ s}^{-1}$  (2–8 keV). Our survey bridges the gap between ultradeep pencil-beam surveys, such as the *Chandra* Deep Fields (CDFs), and shallower, large area surveys, allowing a better probe of the X-ray sources that contribute most of the 2–10 keV cosmic X-ray background (CXB). We find a total of 525 X-ray point sources and 4 extended sources. At  $\sim 10^{-14} \text{ ergs cm}^{-2} \text{ s}^{-1}$  (2–8 keV), our number counts are significantly higher than those of several non-contiguous, large area surveys. Such a large difference is an indication of clustering in the X-ray sources. On the other hand, the integrated flux from the CLASXS field, combined with *ASCA* and *Chandra* ultradeep surveys, is consistent with results from other large area surveys, within the variance of the CXB.

We see spectral evolution in the hardening of the sources at fluxes below  $10^{-14} \text{ ergs cm}^{-2} \text{ s}^{-1}$ , which agrees with previous observations from *Chandra* and *XMM-Newton*. About 1/3 of the sources in the CLASXS field have multiple observations, allowing variability tests. Above  $4 \times 10^{-14} \text{ ergs cm}^{-2} \text{ s}^{-1}$  (0.4–8 keV),  $\sim 60\%$  of the sources are variable. We also investigated the spectral variability of the variable sources. While most show spectral softening with increasing flux, or no significant spectral change, there are a few sources that show a different trend.

Four extended sources in CLASXS is consistent with the previously measured LogN-LogS of galaxy clusters. Using X-ray spectra and optical colors, we argue that 3 of the 4 extended sources are galaxy clusters or galaxy groups. We report the discovery of a gravitational lensing arc associated with one of these sources. Using red sequence and

---

<sup>1</sup>Department of Astronomy, University of Maryland, MD College Park 20742

<sup>2</sup>Laboratory for High Energy Astrophysics, NASA Goddard Space Flight Center, Code 662, Greenbelt, MD 20770

<sup>3</sup>Department of Astronomy, University of Wisconsin, Madison, WI 53706

<sup>4</sup>Department of Physics and Astronomy, University of Hawaii, Honolulu, HI 96822

<sup>5</sup>Institute for Astronomy, University of Hawaii, Honolulu, HI 96822

brightest cluster galaxy methods, we find that the redshifts of the extended sources are in the range  $z \sim 0.5 - 1$ . The inferred masses within the Einstein radii are consistent with the mass profiles of local groups scaled to the same virial radii.

*Subject headings:* cosmology:observations—galaxies:active—X-ray:diffuse background

## 1. Introduction

With several ultra-deep *Chandra* and *XMM-Newton* surveys reaching flux limits as deep as  $f_{2-10 \text{ keV}} \sim 10^{-16} \text{ ergs cm}^{-2} \text{ s}^{-1}$  (Alexander et al. 2003; Giacconi et al. 2002; Hasinger 2003), it is now clear that point sources account for almost all of the X-ray radiation above 2 keV in the universe (Mushotzky et al. 2000; Moretti et al. 2003). These point sources are believed to be primarily active galactic nuclei (AGN), based on their X-ray luminosities. It has also been found that only  $\sim 30\%$  of hard X-ray selected AGN show broad lines in the optical, while  $> 50\%$  appear to be normal galaxies in the optical at the sensitivity limits of the current optical spectroscopic follow-up (e.g., Barger et al. 2001, 2003). In contrast, the soft X-ray selected AGN from *ROSAT* surveys are mostly identified as broad-line AGN in the optical band (Schmidt et al. 1998).

The ultra-deep surveys cover very small solid angles. In the case of the *Chandra* Deep Fields (CDFs), the combined sky coverage is  $\sim 0.2 \text{ deg}^2$ . About 40% variance between fields is seen in the integrated fluxes in the 2 – 8 keV band (Cowie et al. 2002), likely as a result of the underlying large scale structure. To determine the fractional contribution of point sources to the cosmic X-ray background (CXB) with enough accuracy, and to understand how the CXB sources trace the large scale structure, a sufficiently large solid angle is needed. While very large area surveys exist above  $10^{-13} \text{ ergs cm}^{-2} \text{ s}^{-1}$  (2–8 keV) from *ASCA* (Akiyama et al. 2003), the data around  $10^{-14} \text{ ergs cm}^{-2} \text{ s}^{-1}$ , where the point source contribution to the CXB peaks, is limited.

Several intermediate, wide-field, serendipitous *Chandra/XMM-Newton* surveys (Baldi et al. 2002; Kim et al. 2004; Harrison et al. 2003) were designed to increase the solid angle to several degrees at a 2 – 8 keV flux limit of  $10^{-14} \text{ ergs cm}^{-2} \text{ s}^{-1}$ . One of the advantages of such surveys is that they sample randomly across the sky, so the probability of all of them hitting overdense or underdense regions is small. This is useful in determining the normalization of LogN-LogS. On the other hand, serendipitous surveys suffer from the non-uniform observing conditions for each pointing, and in most cases, the pointings contain bright sources. The biases introduced by these non-uniformities are hard to quantify. The serendipitous surveys also have little power in addressing the question of large scale structure traced by X-ray selected AGN, due to the small solid angle of each pointing, sparse and random positions on the sky, and the non-uniformity of the observations. With serendipitous surveys, it is also difficult to perform extensive optical spectroscopic follow-up observations, which are critical in obtaining the redshifts and spectral classifications of the X-ray sources. This is due in part to the advent of large format detectors for imaging and spectroscopy (like those on the Subaru and Keck telescopes), which are more efficient at targeting large-area,

contiguous X-ray surveys, rather than many isolated ACIS-I pointings.

A contiguous, large solid angle survey can compensate for these disadvantages and bridge the gap between the ultradeep “pencil beam” surveys and the large area serendipitous surveys in determining both the normalization of the LogN-LogS and the large scale structure.

In 2001, we began the *Chandra* Large Area Synoptic X-ray Survey (CLASXS) of the multi-wavelength data-rich *ISO* Lockman Hole-Northwest (LHNW) region. The survey currently covers a solid angle of  $\sim 0.4 \text{ deg}^2$  and is sensitive to a factor of 2 – 3 below the “knee” of the 2 – 8 keV LogN-LogS. Such a choice of solid angle and depth maximizes the detection efficiency with *Chandra*. The large solid angle is important for obtaining statistically significant source counts at the “knee” of the LogN-LogS and to test for variance of the number counts on larger solid angles. The choice of solid angle is based on the *ASCA* results that the rms variance of the 2 – 10 keV CXB on a scale of  $0.5 \text{ deg}^2$  is  $\sim 6\%$  (Kushino et al. 2002). The expected variance at the angular scale of our field should be less than the uncertainty of the CXB flux. The uniform nature of the survey allows an unbiased measurement of AGN clustering. We have shown that the field-to-field variance seen between the deep fields can be reproduced within the 9 fields in our survey (Yang et al. 2003; hereafter Yang03).

Our survey region is covered by the deepest 90 and  $170\mu\text{m}$  ISOPHOT observations (Kawara et al. 2004), as well as abundant multiwavelength observations, including the planned *Spitzer Space Telescope (SST)* Wide-Area Infrared Extragalactic Survey (SWIRE). We performed extensive optical follow-up observations using Subaru, CFHT, WIYN, and Keck to obtain multicolor images and spectra of the X-ray sources (Steffen et al. 2004, hereafter Steffen04). These observations provide critical information on the redshifts, spectroscopic classifications and luminosities of the X-ray sources, as well as on the morphologies of the host galaxies. We emphasize that the subarc-second spatial resolution of *Chandra* is critical to allow the unambiguous identification of optical counterparts.

We describe our observations and data analysis methods in §2 and present our X-ray catalog in §3. In §4, we present the X-ray spectral properties and variability of the point sources. In §5, we present our analysis of the extended sources and report on the discovery of a gravitational lensing arc associated with one of the clusters. We summarize the paper in §6. A companion paper by Steffen04 presents our multiwavelength observations and analysis. We will present the spatial correlation functions of the X-ray sources in a subsequent paper. Throughout this paper, we assume  $H_0 = 71$  and a flat universe with  $\Omega_M = 0.27$  and  $\Omega_\Lambda = 0.73$ .

## 2. Observations and Data Reduction

### 2.1. X-ray Observations

We surveyed the LHNW field centered at  $\alpha = 10^h34^m$ ,  $\delta = 57^\circ40'$  (J2000). The region has the lowest Galactic absorption ( $N_H \equiv 5.72 \times 10^{19} \text{ cm}^{-2}$ ; Dickey & Lockman 1990). All 9 ACIS-I observations were obtained with the standard configuration. The pointings are separated from each other by  $10'$  (Figure 1). The fields are labeled LHNW1-9 for reference hereafter. The overlapping of the fields allows a uniform sky coverage, because the sensitivity of the telescope drops significantly at large off-axis angles. Fields LHNW1-3 were observed during April 30th to May 17th 2001, and the rest of the fields were observed during April 29th to May 4th 2002. All fields except LHNW1 have exposure times of  $\sim 40$  ks. LHNW1 is located at the center of the field and has an exposure time of 73 ks. The observations are summarized in Table 1.

We reduced the data with CIAO v2.3 and the calibration files in CALDB v2.20. For our spectral analysis, we updated the data reduction with CIAO v3.01 and CALDB 2.23 to allow the use of CTI corrected calibration files. We followed the CIAO analysis threads (available online at <http://asc.harvard.edu/ciao/>) in reducing the data, including the correction of known aspect problems, CTI problems, and removing high background intervals. Background flares were found in LHNW3 and LHNW6 and have been removed. The resulting event lists were rebinned into 0.4 – 2 keV (soft), 2 – 8 keV (hard), and 0.4 – 8 keV (full) broadband images. Spectral weighted exposure maps were made for each band for each observation, using the observation specified bad pixel files.

### 2.2. Source detection

The detection sensitivity of *Chandra* drops rapidly beyond  $6'$  off-axis. For this reason, we overlapped our ACIS-I fields so that the sensitivity of the survey would be uniform across the field. Since the added signal-to-noise from merging the observations is relatively small, we chose to detect sources in each observation individually and merge the catalogs, rather than to detect sources directly on the merged image. This method certainly loses some sensitivity for very dim sources at some locations. However, since our major interest is to obtain a uniform sample for statistical and follow-up purposes, such a choice is justified. The method also simplifies the source flux extraction because the PSF information could easily be used. Multiple detections of sources in independent observations are very useful for checking and improving the X-ray positions of the sources. Multiple detections also provide an opportunity for measuring the variability of these sources.

From the various detection tools available, we chose to use the *wavdetect* tool included in the CIAO package (Freeman et al. 2002). Since *wavdetect* uses a set of scales to optimize the source detection, the tool is excellent in separating nearby sources in crowded fields. In general, the

method also provides better sensitivity than the classical “sliding box” methods. The drawbacks of *wavdetect* are that it runs rather slowly on large images like the full resolution ACIS-I images, and it requires fine-tuning of the parameters.

We ran *wavdetect* on the full resolution images with wavelet scales of 1,  $\sqrt{2}$ , 2,  $2\sqrt{2}$ , 4,  $4\sqrt{2}$ , 8. Although using larger scale sizes could help to detect very far off-axis sources, it is not very useful for our survey, because of the overlapping of fields. It also increases the computation time to use a large number of scales. We chose to use a significance threshold of  $10^{-7}$ , which translates to a probability of false detection of 0.4 per ACIS-I field based on Monte Carlo simulation results (Freeman et al. 2002).

### 2.3. Source positions

Observations performed before 2002-May-02 suffer from an systematic aspect offset as large as  $2''$  from an error in the pipeline software. This systematic error was carefully calibrated by the *Chandra* X-ray center and corrections are provided. For the affected fields, LHNW1, 2, 3, 4, 5, and 7, we corrected this error following the standard procedures (see *Chandra* analysis thread online at [http://asc.harvard.edu/ciao/threads/arcsec\\_correction/](http://asc.harvard.edu/ciao/threads/arcsec_correction/)).

We further matched the small off-axis X-ray positions reported in each field from *wavdetect* to the optical images. Corrections were then found to maximize the matches. Such corrections are very small. The astrometric improvement also only marginally improved the matching between the X-ray catalogs, thanks to the excellent astrometric accuracy of the instrument. The corrected X-ray catalogs from each observation were then merged (§3.1). A further absolute astrometric correction was applied to the merged X-ray catalog to match to the radio sources in the field. In Figure 2, we show the offsets between the corrected positions and the optical positions for sources in different off-axis angle ranges. Large offsets often occur when the X-ray source is at large off-axis angles. Offsets are generally small, with a dispersion of  $0.23''$  for all the sources detected.

### 2.4. Source fluxes

*Wavdetect* is excellent at detecting sources, but it is not always the best method for flux extraction. Three issues could contribute to an incorrect estimation of source counts in *wavdetect*. First, the flux measurements in *wavdetect* use a monochromatic PSF size, which, by default, corresponds to an enclosed energy of 0.393 at the energy of choice, or the  $1\sigma$  integrated volume of a normalized two-dimensional Gaussian. Though this parameter is adjustable, larger enclosed energy values could cause confusion of close sources. Since the construction of source cells is carried out by convolving the source image with wavelet functions, the “smearing” effects of the convolution can in general make the source cell large enough to include most of the source photons, but the fraction of the flux recovered varies from source to source. Second, due to the statistical fluctuations in

the source photon distribution, some sources show multiple peaks in the convolved image. Unless perfect PSF information is available, randomness should exist in determining which peak belongs to a single source. This problem is particularly severe when the source is very off-axis and the PSF shape cannot be approximated by a Gaussian. The third issue is the background determination, a problem other methods also share. The background in *wavdetect* is obtained in the immediate neighborhood of the source. This is useful because of the known large background fluctuations. However, if the background is drawn too close to the source, the PSF wing would likely be taken as background. This could result in an over-subtraction of the background and lead to underestimated source counts. This effect is seen in a correlation of source counts with background density in the *wavdetect* results. All of these issues would lead to an underestimation of source counts. This has been noticed in the analysis of the deep *Chandra* fields (Giacconi et al. 2002; Hornschemeier, private communication).

Because of the spectral differences of the sources and the sensitivity differences between energy bands, sources detected in one band are not always detected in another at high significance. There is no simple way within *wavdetect* to provide upper limits for these sources. To obtain the source fluxes or upper limits in the non-detection band, an alternative flux extraction method is needed.

For these reasons, we wrote an aperture photometry tool for source flux extraction. The method uses a simple circular aperture which matches the size of the PSF. To do this, we first compared the broadband PSFs derived from our observations with the PSF size file provided with CIAO, as described below.

#### 2.4.1. Broadband PSFs

Both the PSF library used by the CIAO tool *mkpsf* and the circularly averaged PSFs used by the detection codes (*psfsize20010416.fits*) are generated at monochromatic energies using simulations of the telescope. Spectral weighted average energy is usually used for selecting the PSF file for broadband images. Since the spectra of the X-ray sources are mostly unknown, an average spectrum has to be assumed. Whether such selected PSFs agree with the observed broadband PSFs needs to be tested. We constructed “average PSFs” for different off-axis angles using sources which have no neighbors within  $40''$  in our 9 observations (Figure 3). It should be noted that these PSFs are inaccurate at large scales because the PSF wings, which span more than  $1'$ , could not be well determined in these observations. The source images from the same off-axis annuli are stacked, and the curves-of-growth are constructed. The background regions are fitted with quadratic forms using nonlinear least-square fits. To compare with the library PSFs used by *wavdetect*, we linearly interpolated the library PSFs to the off-axis angles and the spectral weighted averaged energies. To account for the fact that part of the PSF wings had been fitted as background in our data, we did the same “background fitting” on the interpolated PSFs. This allows a comparison of the observed curve with the interpolated PSF. The broadband PSFs are generally narrower than the interpolated PSFs, except for one case in the hard band where the off-axis angle is large.

### 2.4.2. Aperture photometry

We performed our flux extractions in the following way. We used circular extraction cells, choosing the radius of cells from the PSF library at a nominal enclosed energy of  $\sim 95\%$  (the true enclosed energy should be  $>95\%$  based on the discussion above) if the cell size is  $> 2.5''$ . For source close to the aim point, a fixed  $2.5''$  radius was used. The background is estimated in an annulus region with an area 4 times as big as the source cell area, with inner radius  $5''$  larger than the source cell radius. To avoid nearby sources being included in the background region, the background region is divided into 8 equal-sized segments (Figure 4). The mean background counts are estimated, excluding the segment which contains the highest number of events. Then the  $3\sigma$  Poisson upper limit is derived using the approximations provided in Gehrels (1986). The background is then recalculated with only the background segments that contain counts less than the upper limit. The net counts are obtained by subtracting the background from the source counts within the source cell. We compare the obtained net counts with the net counts obtained with *wavdetect* (Figure 5). While they mostly agree, the source photons derived from our method are, on average, higher than those from *wavdetect*, especially for low-count sources. The average increases are 4%, 7%, and 8% for the soft, full, and hard bands, respectively. We hand-checked the sources with large discrepancies from the two methods, and we found our estimates to be more reliable.

### 2.4.3. Exposure time and flux conversion

The prerequisite for using exposure maps is that the effective area is only weakly dependent on energy. This is not the case for our broadband images, where the effective area changes rapidly with energy. Using exposure maps blindly, even the spectrally weighted ones, will inevitably introduce large errors in the resulting fluxes. However, the vignetting (the positional changes of sensitivity) is less sensitive to energy. In other words, if we normalize the exposure maps obtained at different energies to the aim points, then the differences between such “normalized exposure maps” are very small.

Based on this fact, we use the exposure maps only to correct for vignetting and compute the flux conversion at the aim point using spectral modeling. We first make full resolution spectrally weighted exposure maps (using monochromatic maps do not change the results significantly). For each source, the exposure map is convolved with the PSF generated using *mkpsf* and normalized to the exposure time at the aim point. This is the effective exposure time if the source is at the aim point.

The conversion factor is then obtained at the aim point by assuming the source has a galactic, absorbed, single power-law spectrum. The power-law index is calculated using the hardness ratio of each source, defined as  $HR \equiv C_{hard}/C_{soft}$ , where  $C_{hard}$  and  $C_{soft}$  are the count rates in the hard and soft bands. XSPEC was used in computing the conversion from  $HR$  to  $\Gamma$  and for calculating

the conversions. The degradation of quantum efficiency during the flight of the observatory has been accounted for using the standard procedure.

### 3. Catalog

#### 3.1. Merging Catalogs

We first merged the three band catalogs. We used a  $3\sigma$  error ellipse from the *wavdetect* output as the identification cell. Flux extraction was then performed on all entries in the merged catalogs in all bands using the best position of the sources. We compared the three band catalogs with the optical catalog to find the astrometric corrections for each observation, as described in §2.3. The nine catalogs were then merged. The fluxes of the sources with more than one detection in the 9 fields were taken from the observation in which the effective area of the source was the largest, except for those sources with more than 2 detections having normalized areas  $> 80\%$ , where we took the averaged flux. We visually checked the final catalog to ensure the correctness of the merging process. The final catalog contains 525 sources.

The distribution of the source off-axis angles in the merged catalog is shown in Figure 6. It can be seen that most of the sources fall within the  $< 6'$  range. Figure 7 shows the distribution of sources with multiple detections. About 1/3 of the sources have more than one observation.

#### 3.2. Column-by-column description of the catalog

We present the final catalog in two tables (Table 2a and Table 2b). In Table 2a, we list the source positions, fluxes, and hardness ratios. In Table 2b, we list the source net counts, effective exposures, and detection information.

**Table 2a: Basic properties**

**Column 1:** Source number used in the catalog. The numbers correspond to ascending order of right ascension.

**Column 2:** Source name follows the IAU convention and should read CXCLASXS, plus the name given in the table.

**Columns 3 – 4:** The X-ray position, corrected for the aspect errors of the telescope, if applicable, and for the general astrometric solution by comparing with the optical images (see §2.3). For sources with multiple detections in the three bands and the 9 observations, the best position is taken.

**Columns 5 – 6:** Statistical error of the X-ray position quoted from the *wavdetect* lists.

**Columns 7 – 9 :** X-ray fluxes in the soft, hard, and full bands in units of  $10^{-15}$  ergs  $\text{cm}^{-2}$   $\text{s}^{-1}$ . If a source is detected in multiple observations, and if there are more than one observation in which the source effective area is more than 80% of the effective area at the aim point, then the mean flux is used; otherwise, the flux from the observation that has the largest effective area is used. The errors quoted are the  $1\sigma$  upper and lower limits, using the approximations from Gehrels (1986). For any source detected in one band but with a very weak signal in another, the background subtracted flux could be negative. In this case, only the upper limit is quoted.

**Columns 10:** Hardness ratio as defined in §2.4.3. The upper or lower limit is listed for a source with no net extracted photons in the soft or hard bands.

**Table 2b: Additional Properties**

**Column 1:** Source number.

**Columns 2–4:** Net counts in the soft, hard, and full bands. If a source is detected in multiple observations, then the observation in which the source has the largest effective area (see Column 8) is used. As in Table 2a, for the sources with negative counts, only the upper limits are listed.

**Columns 5–7:** Effective exposure time in each of the three energy bands from the exposure map.

**Columns 8–9:** Detection information. Column 8 is the LHNW field number where the source has the largest effective area. Column 9 lists the LHNW field numbers (each digit represents a field number) in which the source has been detected in at least one of the three bands. Sources with multiple detections are necessary for the detection of variability (see §5.2).

## 4. Results

### 4.1. Number counts

#### 4.1.1. Incompleteness and Eddington Bias

Incompleteness can be caused by energy or positional dependence of the sensitivity of X-ray telescopes. Because the spectrum of a source carries important information on the physical nature of the source itself, sources of different spectra are usually categorized as different types. The energy dependent sensitivity acts like a filter in selecting “hard” and “soft” types of X-ray sources. The soft band detected sources always contain more soft spectrum objects than the hard band detected sources and *vice versa*. Unless the fraction of each type remains constant for all fluxes (which we now know is not true), the energy dependent incompleteness cannot be easily corrected. This issue is very important in interpreting the fraction of different types of objects in flux limited surveys. It is desirable to obtain number counts for each type of source, but it is hard to do that for the CXB sources, because the spectra are hard to determine. For our medium deep survey, it is sensible to

follow tradition and only discuss the number counts in energy bands.

The positional dependent incompleteness is caused by vignetting and aberration of the X-ray optics. The vignetting causes the effective area to drop with off-axis angle, and the aberration makes the off-axis PSF larger so that it includes a larger number of background events in the source cell. The net effect is that the sensitivity of source detection drops with increasing off-axis angle. The sky area is therefore flux dependent.

These effects can be investigated via Monte Carlo simulations. We first generated background images using observations of fields #1 and #4, which represent the 70 ks and 40 ks exposures. Point sources are removed from the images, and the holes left in the images are filled by sampling the local background. Random sources are generated uniformly on the background images. The fluxes of the sources are generated by randomly sampling a complete subset of the combined *Chandra* Deep Fields catalog (Alexander et al. 2003). The subset contains only sources with hard band fluxes  $> 5 \times 10^{-16}$  ergs cm $^{-2}$  s $^{-1}$  and effective exposure times  $> 200$  ks. The input fluxes are converted to on-axis counts assuming power-law spectra with  $\Gamma = 1.4$ . The exposure map for each image is consulted to find the vignetting effect at the source location, and the normalized exposure is multiplied by the true counts to obtain the “observed” net counts. Only sources with more than 3 counts are used in the simulation to avoid adding too many undetectable dim sources to the background. We use the CIAO tool *mkpsf* to generate realistic source shapes at the source positions and energies. The PSF is then sampled to have the same number of photons as in the source. We chose to use *mkpsf* instead of using the *Chandra* simulator MARX because we find the PSF library used by *mkpsf* better resembles sources at large off-axis angles. The number density of the sources is chosen to be 2 times higher than the observed density to increase the number of simulated sources without affecting detections. We ran 100 simulations on the 2 fields and the three energy bands and detected the sources using *wavdetect* with identical parameter settings to those we used in preparing the observed catalog. Because of the large computation time, the number of simulations that can be done is limited.

We then compared the output catalogs with the input source catalogs. Because of the small size of the simulation, the completeness within  $4''$  is not well determined, and a 5% uncertainty exists in the determined fractions. Fortunately, the PSF effect is small at such small off-axis angles. For a given flux threshold, the fraction of source detections drops monotonically with off-axis angle. This relation is fitted between  $4'$  and  $10'$  with a linear least-squares fit. The 95% complete off-axis angle limit is then taken from the interpolation of the fit. The resulting flux thresholds versus off-axis radii are shown for the three bands and the two exposure times in Figure 8. We note that at large off-axis angles, the sensitivity drops rapidly. This is due to the choice of wavelet scales. When the largest scale used becomes smaller than the PSF size of the source, *wavdetect* is no longer sensitive. This effect, however, is not important for our observations, because most of the sources of interest are within  $6'$  off-axis, thanks to the overlapping of fields. With these curves, we are able to make threshold maps for the combined catalogs of all three bands. Sources at very large off-axis angles are excluded from the study of the LogN-LogS. The combined solid angle versus flux

thresholds is shown in Figure 9.

The Poisson fluctuations in the source fluxes could result in an overestimation of number counts close to the detection limits. This is known as the Eddington Bias. The effect depends both on the slope of the LogN-LogS and the level of fluctuation. For the CLASXS field, the detection threshold is below the “knee” of the LogN-LogS, and the Eddington bias is relatively small. We corrected this bias using the method described in Viklinin et al. (1995). In Figure 10, we compare the average input flux with the average output flux at different off-axis angles from the simulations. For the soft band, the correction is only important below  $2 \times 10^{-15}$  ergs cm<sup>-2</sup> s<sup>-1</sup>. For the hard band, the correction is important below  $8 \times 10^{-15}$  ergs cm<sup>-2</sup> s<sup>-1</sup>. We fit flux–flux curves in Figure 10 for the different off-axis angles with fourth order polynomials and correct the source fluxes in the observed catalog using these fits.

#### 4.1.2. Number counts

Sources are selected by consulting the threshold map at the source positions and including only those with Eddington bias corrected fluxes higher than the threshold map values. Sources very far off-axis are excluded from the analysis. With these selections, we used a total of 310 and 235 sources in the soft and hard bands, respectively, to construct the LogN-LogS. The cumulative LogN-LogS relations are computed using the formula

$$N(> S) = \sum_{S_i > S} \frac{1}{\Omega(S_i)}, \quad (1)$$

where  $\Omega$  is the complete solid angle. We show the results in Figure 11 in the soft and hard bands with  $1\sigma$  Poisson errors. The differential LogN-LogS for the two bands are shown in Figure 12, which are calculated using the formula

$$\frac{dN}{dS} = \sum \frac{1}{\Omega_i \Delta S}, \quad (2)$$

in units of deg<sup>-2</sup> per  $10^{-15}$  ergs cm<sup>-2</sup> s<sup>-1</sup>. We fit the resulting differential number counts with single or broken power laws in the form of

$$\frac{dN}{dS} = n_0 \left( \frac{S}{10^{-14}} \right)^{-\alpha} \quad (3)$$

using error weighted least-square fits. Since our survey best samples the “knee” of the LogN-LogS, the slope of the power-laws are not well constrained due to the lack of data points both far above and below the “knee”. On the other hand,  $n_0$  is better determined, to within 1%.

For the soft band, we fit the number counts between  $10^{-15}$  and  $10^{-14}$  ergs cm<sup>-2</sup> s<sup>-1</sup> with a power law. We find the best-fit parameters to be  $\alpha = 1.7 \pm 0.2$  and  $n_0 = 12.49 \pm 0.02$ . The slope is in good agreement with previous observations, such as the *Chandra* Deep Field-North ( $1.6 \pm 0.1$ ,

Brandt et al. 2001), SSA13 ( $1.7 \pm 0.2$ , Mushotzky et al. 2000), and the compiled wide fields from *Chandra*, *XMM-Newton*, *ROSAT*, and *ASCA* ( $1.60_{-0.03}^{+0.02}$ , Moretti et al. 2003; hereafter, Moretti03). The normalization also shows excellent agreement with the compiled results from the large area survey of Moretti03, which has an effective solid angle at  $10^{-14}$  ergs cm $^{-2}$  s $^{-1}$  larger than that of CLASXS. Above  $10^{-14}$  ergs cm $^{-2}$  s $^{-1}$ , the slope steepens, but the fluctuations in the number counts make it difficult to find a reasonable fit. However, the LogN-LogS is apparently consistent with a slope of  $\alpha = 2.5$ , shown as the dotted line at these fluxes.

Similarly, we model the hard band number counts with a broken power law and obtain the following best-fit parameters. For  $S > 10^{-14}$  ergs cm $^{-2}$  s $^{-1}$ ,  $\alpha = 2.4 \pm 0.6$  and  $n_0 = 45.6 \pm 0.5$ ; for  $3 \times 10^{-15} < S < 2 \times 10^{-14}$  ergs cm $^{-2}$  s $^{-1}$ ,  $\alpha = 1.65 \pm 0.4$  and  $n_0 = 38.1 \pm 0.2$ . For comparison, we also plot the best-fit cumulative LogN-LogS from Moretti03 and differential LogN-LogS from the SEXSI fields (Harrison et al. 2003) and from Cowie et al. (2002). At fluxes below  $8 \times 10^{-15}$  ergs cm $^{-2}$  s $^{-1}$ , the differential LogN-LogS for all the fields agrees within the errors. The difference in the total counts at a flux limit between the CLASXS field and the Moretti03 fields is also small. An apparent difference is seen around  $10^{-14}$  ergs cm $^{-2}$  s $^{-1}$ : the total counts at  $10^{-14}$  ergs cm $^{-2}$  s $^{-1}$  are  $\sim 70\%$  higher than those from Moretti03. This is significant at greater than the  $3\sigma$  level.

The integrated flux between  $3 \times 10^{-15}$  and  $8 \times 10^{-14}$  ergs cm $^{-2}$  s $^{-1}$  from the LogN-LogS is  $(1.2 \pm 0.1) \times 10^{-11}$  ergs cm $^{-2}$  s $^{-1}$  deg $^{-2}$ . This is  $\sim 20\%$  higher than that from Moretti03 and SEXSI in the same flux range. Since there is little difference in the number counts between the CLASXS fields and the other large solid angle surveys at fluxes lower than  $8 \times 10^{-15}$  ergs cm $^{-2}$  s $^{-1}$ , we should expect little difference below the survey limit on the same angular scales. If integrated to lower fluxes, and including the integration from *ASCA* above  $8 \times 10^{-14}$  ergs cm $^{-2}$  s $^{-1}$ , the fractional difference between the CLASXS field and the other large solid angle surveys can be reduced to  $\sim 10\%$  without considering the possible biases. This difference is higher than expected from the variance in the CXB from *ASCA* observations but is consistent with recent observations with *RXTE/PCA*, where a 7% variance is seen among several  $\sim 1$  deg $^2$  fields (Revnitsev et al. 2003).

The uncertainty of the hard CXB itself is  $\sim 10 - 15\%$ . The differences in the integrated point source fluxes from various large fields are within this uncertainty. In terms of the true contribution from point sources to the CXB, a field with a solid angle of  $\sim 0.3$  deg $^2$  seems to be large enough to be representative.

The detection of the large variance in the hard band source counts around  $10^{-14}$  ergs cm $^{-2}$  s $^{-1}$  on our survey scale seems to indicate that the sources that emerge at this flux are more clustered on the sky than the soft band selected sources. These sources could account for most of the cosmic variance observed. This issue will be discussed in a separate paper.

## 4.2. Spectral properties and variability of the CXB sources

### 4.2.1. Hardness ratio

We employ a hardness ratio (§2.4.3) to quantify statistically the spectra of the CXB sources in our field. Figure 13 shows the distribution of hardness ratio versus full band flux. We have also marked the hypothetical photon indices ( $\Gamma$ ), assuming the hardness ratio change is purely due to the slope change of a single power-law spectrum. At fluxes  $> 3 \times 10^{-14}$  ergs cm $^{-2}$  s $^{-1}$ , most sources cluster around  $\Gamma \sim 1.7$ . At lower fluxes, the hardness ratio distribution scatter increases and the relative number of hard sources increases. Below  $3 \times 10^{-15}$  ergs cm $^{-2}$  s $^{-1}$ , the data show a paucity of hard sources. This is a selection effect caused by the sensitivity in the hard band being lower than in the soft band for most spectra. We stacked the sources in flux bins and calculated the hardness ratios of the stacked spectra. Figure 14 shows the stacked hardness ratios from both the CLASXS  $> 10^{-14}$  ergs cm $^{-2}$  s $^{-1}$  sample and the combined CDFs  $> 10^{-15}$  ergs cm $^{-2}$  s $^{-1}$  sample. The flux thresholds are chosen to avoid selection effects caused by the sensitivity differences between the soft and hard bands. It is apparent that the results from our data and those from the CDFs agree well.

The spectral flattening at low fluxes has been observed by several authors (e.g., Mushotzky et al. 2000; Tozzi et al. 2001; Piconcelli et al. 2003; Alexander et al. 2003) with observations of different depths. Spectral analyses with *XMM-Newton* observations indicate that such a flattening is mainly caused by absorption. These obscured AGN must dominate the population around the “knee” of the LogN-LogS to account for the flat spectrum of the CXB. Since most of the *XMM-Newton* spectral observations have reached a few times  $10^{-14}$  ergs cm $^{-2}$  s $^{-1}$  (Piconcelli et al. 2002), and the mean spectrum at this threshold is still too soft compared with that of the CXB, a sharp increase of obscuration or a change of spectral shape at a flux  $\sim 10^{-14}$  ergs cm $^{-2}$  s $^{-1}$  is inevitable. Such a sharp change is seen in the change of hardness ratio in our wide-field sample.

### 4.2.2. Variability

X-ray variability is an important factor in distinguishing AGN from starburst galaxies. Almost all AGN vary in X-rays, except those sources which are Compton thick. Alexander et al. (2001) showed that only a small fraction of the optically faint X-ray sources vary. Possible explanations could be that a large fraction of the optically faint sources are Compton thick, or that the amplitude of variation of the optically faint sources is much lower than that of the broad and/or narrow-line AGN at the same flux thresholds.

We examine the variability of sources that have been detected in more than one of our observations. Since the observations were taken in two groups, separated by about one year, and each group of observations were taken within a few days (see Table 1), we are able to test variability on timescales of days and/or one year, depending on the location of the source.

For timing analyses with low counts per bin, the usual  $\chi^2$  statistic is inadequate. We use the  $C$ -statistic (Cash 1979) in testing the significance of variability. Cash (1979) showed that the  $C$ -statistic (a reduced form of likelihood ratio) written as

$$\Delta C = -2 \sum_{i=1}^N [n_i \ln(e_i) - e_i - n_i \ln(n_i) + n_i] \quad (4)$$

is asymptotic to a  $\chi^2$  distribution with  $N - 1$  degrees of freedom, where  $n_i$  is the observed counts in the  $i$ th sample,  $e_i$  is the expected counts in that sample, and  $N$  is the total number of samples used. We restricted the sample for the variability test to sources with expected counts greater than 10 in all observations. The null hypothesis rejection probability was chosen to be 0.01.

A total of 168 sources were tested for variability, of which 42 sources are significantly variable and 28 sources show variability on timescales of days. There are 29, 16, and 30 variable sources detected in the soft, hard, and full bands, respectively. Figure 15 shows the light-curves of the sources that were tested to be variable in any of the three energy bands. In the top panel of Figure 16, we show the fraction of variable sources detected versus flux. Between  $4 - 8 \times 10^{-14}$  ergs cm $^{-2}$  s $^{-1}$ , 70% of the sources tested show variability. This fraction drops dramatically as the flux decreases and, at  $10^{-14}$  ergs cm $^{-2}$  s $^{-1}$ , reaches below 20%. This is at least in part due to the selection effect that larger variability is needed at lower fluxes to make the test significant. At fluxes above  $8 \times 10^{-14}$  ergs cm $^{-2}$  s $^{-1}$ , only one of the four sources tested (25%) was found to be variable.

Following Nandra et al. (1997), we define the magnitude of variability as the “excess variance”, the error subtracted  $rms$  variance

$$\sigma_{rms}^2 = \frac{1}{N\mu^2} \sum_{i=1}^N [(f_i - \mu)^2 - \sigma_i^2], \quad (5)$$

where  $f_i$  is the flux in each observation,  $\mu$  is the mean of the fluxes, and  $\sigma_i$  is the Poisson error of the flux. By assuming the same power density spectrum of X-ray variability for all AGN,  $\sigma_{rms}^2$  can be used as a good indicator of whether the variability exceeds the Poisson noise. It has been found that there exists a good anti-correlation between  $\sigma_{rms}^2$  and AGN luminosity (Nandra et al. 1997) in local AGN samples.

In Figure 17, we show the excess variance of sources that had been detected to be variable versus X-ray flux in the three energy bands. At high fluxes, the average  $\sigma_{rms}^2$  is significantly lower than at lower fluxes. As mentioned above, variability is harder to detect for low flux sources, unless the source is more variable than that of the brighter sources, so this bias could explain why there are very few low flux, low variability sources in the plot. In addition, the sources we detect to be variable are generally soft. This is consistent with the observation from the CDFs that optically faint sources (most of which are hard spectrum AGN) are less variable (Alexander et al. 2001).

#### 4.2.3. Spectral variability

Very little is known about the spectral variability of the sources that contribute the most to the CXB due to a lack of data. Spectral variability is seen in about half of the well-studied brighter sources, with a general trend of softening of the 2 – 10 keV spectra with increasing source intensity. But a counterexample is NGC7469, where the spectrum flattens when the source flux increases (Barr 1986). The variability could be accounted for either with a change in the relative normalization of the different spectral components or by variation in the absorption.

In Figure 18, we show hardness ratios versus full band fluxes for the variable sources. While most of the sources show either no clear spectral variability, or a trend of spectral softening with increasing flux, there are a number of sources that clearly become harder with increasing flux. There are also a few sources that exhibit a mixed trend. On average, these sources tend to have softer spectra with increasing flux.

## 5. Extended Sources

### 5.1. Detection

We searched the 0.4–2 keV images of each observation for extended sources using the *vtpdetect* tool provided in CIAO. The method uses Voronoi tessellation and percolation to identify dense regions above Poisson noise. This method performs best on smooth overdense regions but could confuse crowded point sources. We chose to use a threshold scale factor of 0.8 and a maximum probability of false detection of  $10^{-6}$  and to restrict the number of events per source to  $> 30$ . We used default values for the rest of the parameters. This choice of parameters maximizes the detection of low surface brightness sources at high significance. We visually examined the source list to screen out apparent blended point sources. The candidates were then selected by comparing the 99% PSF radius with the equivalent radius of the source region, and only sources with a PSF ratio (defined as  $\sqrt{(A/\pi)}/r_{99}$ , where  $A$  is the area of the source region reported by *vtpdetect*, and  $r_{99}$  is the 99% PSF radius at the off-axis angle) higher than 10 were considered extended (Table 3).

Four sources were found to be significantly extended, and all but Source 3 have an off-axis angle of  $< 5'$  in the X-ray observations. Source 3 is at an off-axis angle of  $8.4'$ . With the X-ray image alone, one could not rule out the source being a blend of point sources. However, a bright gravitational lensing arc found in the optical image (see §5.6) at the X-ray peak makes it very likely that the X-ray emission is associated with a cluster. Considering the non-uniformity of the detection due to vignetting and PSF effects, the number counts for extended sources above  $3.7 \times 10^{-15}$  ergs cm $^{-2}$  s $^{-1}$  are roughly  $> 10$  deg $^{-2}$ . This agrees with the LogN-LogS of clusters at these fluxes found in the CDFs (Bauer et al. 2002). It is interesting to note that all 4 extended sources are found on only two of the overlapping ACIS-I fields in the north of the LHNW region.

## 5.2. Optical imaging observations

Optical observations are describe in detail in Steffen04. Optical images were obtained with Suprime-Cam on Subaru (in  $B, V, R, I, z'$ ) and with the CFH12K camera on the Canada-France-Hawaii Telescope (CFHT; in  $R, B$ , and CFHT  $z'$ ). The  $2\sigma$  limits in  $B, V, R, I$ , and  $z'$  are 27.8, 27.5, 27.9, 26.4, and 26.2.

X-ray contours overlaid on  $R$  band optical images are shown in Figure 19. We examined the number counts of galaxies within circular cells with fixed radii of  $0.5'$ . At a threshold of  $R < 24$ , a total of 19, 28, 18, and 9 galaxies were found within the cells centered at the X-ray peaks of each extended source. Because a star is found at  $0.6'$  south-east of the X-ray peak of Source 2, the galaxy counts could be underestimated. Compared with the expected 6.7 galaxies per cell obtained from the whole field, the overdensities of galaxies in Sources 1 and 2 are  $> 3\sigma$ , while the overdensity of galaxies in Source 3 is  $\sim 3\sigma$ . Source 4 does not show significant clustering of galaxies in the  $R$  band image. Sources 1 and 2 are very close to each other, with a separation of  $\sim 2'$ . The closeness and the elongated morphology of the two sources suggest that they are undergoing interactions. Source 3 is extended along the east-west direction with multiple peaks. All 4 sources show bright elliptical galaxies at the X-ray peaks.

## 5.3. X-ray spectra

We extract very coarse spectra (grouped to  $> 15$  counts per bin to allow the use of the  $\chi^2$  statistic) and attempt to constrain the properties of the clusters. We fit the data with a simple MEKAL model in XSPEC (v11.2), with a fixed abundance of 0.3 of the solar value and a fixed Galactic absorption. We restrict the spectral fitting to within  $0.5 - 5$  keV, because the signal-to-noise ratio is poor outside of this range.

The source extraction and background regions of Sources 1 and 2 are shown in Figure 20. The regions avoid the point sources between the two clusters. The spectra are shown in Figure 21. For Source 1, we found the best fit to be  $kT = 1.4_{-0.2}^{+1.0}$  keV and  $a = 0.5_{-0.2}^{+0.2}$ , with a reduced  $\chi^2 = 8.8$  for 9 degrees of freedom. This agrees with the redshift estimates using the optical data (Table 4). Fitting the same model to the spectrum of Source 2 with the redshift fixed to  $z = 0.5$  yields  $kT = 3.1_{-1.6}^{+13.5}$  keV, with a reduced  $\chi^2 = 4.6$  for 9 degrees of freedom. The constraint on the temperature is poor, but the probability that the temperature of Source 2 is significantly different than that of Source 1 is low. This can be seen in Figure 22, where the joint probability contour of the temperature from the two sources is shown. The confidence level for the two sources having different temperatures is only  $2\sigma$ . Combining the two data sets and fixing  $z = 0.5$ , we find  $kT = 1.7_{-0.5}^{+2.2}$  keV.

The spectrum of Source 3 shown in Figure 23 was extracted from a circular region with radius  $36''$ . The background was extracted from an annulus with inner radius  $36''$  and outer radius  $60''$ .

The data cannot constrain the model very well, but a simple fit with an absorbed power-law shows that the spectrum is very soft with photon index  $\Gamma = 2.6$  and reduced  $\chi^2 = 7.2$  for 7 degrees of freedom. Fitting with a MEKAL model and assuming a redshift of  $z = 1.1$  (see §5.5), we obtain a temperature of  $2.3_{-0.8}^{+1.1}$  with reduced  $\chi^2 = 0.77$ . The temperature is insensitive to the redshift between  $z = 0.4 - 1.4$ . The fact that the MEKAL model fits the data better makes it less likely that Source 3 is a blend of several point sources.

With only 30.7 net counts, it is impossible to model the spectrum for Source 4. However, the source has very few counts above 2 keV, indicating that the temperature should be low if the source is at  $z > 0.4$ , as implied from the optical data.

The virial masses of the extended sources can be roughly estimated using the best-fit  $M - L$  relation (Finoguenov et al. 2001),  $M_{500} = 2.45 \times 10^{13} T^{1.87}$ , where  $M_{500}$  is the mass within a radius where the overdensity is 500. The results are shown in Table 5. All of the sources belong to low mass clusters or groups, and this result is not very sensitive to the redshift because of the very soft spectra.

#### 5.4. Angular sizes

The angular sizes of the sources were quantified by the widths of the radial profiles. We fitted the radial profiles of the sources with integrated 2-D Gaussian curves, which describe the low S/N ratio data reasonably well. We constructed the cumulative counts as a function of off-source radius (curve-of-growth). Exposure maps were applied to correct for vignetting. Nearby point sources were removed and replaced with background noise. The background regions were selected visually and fitted with a quadratic form plus a constant. The curves-of-growth were then normalized to the best-fit backgrounds. The normalized curve-of-growth for each source is shown in Figure 24. This left only one parameter to be determined—the widths of the curves. The best-fit  $1\sigma$  radii are listed in Table 5.

#### 5.5. Redshifts

We infer the redshifts of the extended sources using the red sequence method, as well as the brightest cluster galaxy (BCG) method. Based on observations of clusters, there is usually a population of early-type galaxies which follow a color-magnitude relation (red sequence). This relation changes with redshift in a predictable way, such that a robust two-color photometric redshift can be obtained (Gladders & Yee 2000). Color-magnitude plots of the sources within  $0.5'$  of the X-ray centers are shown for each extended source in Figure 25. Red sequences can be clearly seen in Sources 1, 2, and 4. By comparing with the models from Yee & Gladders (2001), we can estimate the redshifts for these three extended sources (Table 4). Source 3 does not show a clear red sequence.

BCGs are often used as distance indicators, because they have almost constant luminosity (Humason, Mayall, & Sandage 1956). One of the difficulties in applying this method is that with optical images alone, it is hard to distinguish between the background and the cluster members, unless a density peak can be clearly determined. In our case, this is less worrisome because bright spheroidal/lenticular galaxies are found at the X-ray peaks of all of the extended sources. This clearly associates these galaxies with the clusters. Furthermore, these galaxies are also the brightest early-type galaxies in the regions where X-ray emission is significant. Following Postman & Lauer (1995), we fit the radial profile of each of the BCGs to obtain the magnitudes within angular radius  $r_m$  and the slope of the profile ( $\alpha \equiv d\log L_m/d\log r|_{r_m}$ , where  $L_m$  is the luminosity within  $r_m$ ). We eye examine the profile so that nearby galaxies are not included in the aperture. K correction is performed using  $K_R = 2.5\log_{10}(1 + 0.96z)$ . We then solve the redshifts for each galaxy by assuming the cosmological parameters in §1. The resulting redshifts are listed in Table 4.

While it appears that the BCG method produces higher redshifts than the red sequence method, the differences are not significant, given the large uncertainties in both methods. The redshifts of Sources 1 and 2 also agree with the spectral fitting results from the X-ray data.

The X-ray luminosities of the extended sources are listed in Table 5, assuming the red sequence-determined redshifts except for Source 3, where BCG redshift is adopted. Within errors, the temperatures and luminosities of the sources agree with the scaling law found in high-redshift X-ray clusters (Ettori et al. 2003), but the constraint is weak.

### 5.6. Discovery of a gravitational lensing arc

We have found a gravitational lensing arc close to Source 3 (Figure 26). The arc has an angular radius of  $\sim 6''$ . A bright spheroidal galaxy is clearly associated with the arc. A possible counter arc is seen connecting to the west of the bright galaxy but is not fully resolved. With  $B, V, R, I$ , and  $z'$  observations, we can estimate photometric redshifts for the cD galaxy and the arc using the publicly available photometric redshift code Hyperz (Bolzonella et al. 2000). We find photometric redshifts for the cD galaxy and the arc of  $z = 0.45$  and  $z = 1.7$ , respectively. The redshift of the galaxy is slightly different than the redshift of the cluster obtained using the BCG method. From our experience, one often needs at least 7 colors to obtain a secure photometric redshift. The redshift estimates therefore need verification. We now discuss the estimated lensing properties.

If the source is at  $z_{src} \sim 0.45$  and the arc is at  $z_{arc} \sim 1.7$ , then we can estimate the mass within the Einstein radius (reasonably approximated by the radius of the arc) as

$$M(\theta < \theta_E) = 1.1 \times 10^{14} \left(\frac{\theta}{30''}\right)^2 \left(\frac{D_{LS}D_L}{D_S}\right) M_\odot, \quad (6)$$

where  $D_L$ ,  $D_S$ , and  $D_{LS}$  are, respectively, the angular diameter distances (in units of Gpc) of the lens, source, and the distance between the lens and source. With  $z_{src} \sim 0.45$  and  $z_{arc} \sim 1.7$ , we obtain  $M(\theta < \theta_E) \sim 3.3 \times 10^{12} M_\odot$ . We compare this mass with what would be expected if

the source were a group of galaxies at  $z = 0.45$ , assuming the mass profiles are self-similar. By fixing the redshift, the X-ray spectra yield a temperature of 2.2 keV. The virial radius is roughly  $r_{500} = 0.63 \times \sqrt{kT} = 955$  kpc (Finoguenov et al. 2001), where  $r_{500}$  is defined as the radius within which the overdensity is 500. The size of the arc at  $z \sim 0.45$  is  $r_{arc} \sim 37$  kpc  $= 0.036r_{500}$ . Comparing with the mass profiles of NGC2563, NGC4325, and NGC2300 (Mushotzky et al. 2003), the mass inside the Einstein radius agrees very well with that of a group of galaxies. The virial mass of the group can then be estimated to be  $\sim 1.2 \times 10^{14} M_{\odot}$  (Finoguenov et al. 2001).

If the cluster is at  $z \sim 0.7$ , as implied from the BCG method, and if the best-fit temperature  $kT = 0.23$  keV is assumed, then we can search for the best redshift of the lensed galaxy, so that the mass within the Einstein radius agrees with the mass profile of groups. We find that if the lensed galaxy is at  $z = 1.8$ , then the mass within the Einstein radius is  $M(\theta < \theta_E) \sim 3 \times 10^{12} M_{\odot}$ , which fits the mass profile of groups.

If the redshift estimate is correct, then the arc system is very similar to the one discovered in the *ROSAT* deep survey of the Lockman Hole (Hasinger et al. 1998b). High-redshift gravitational lensing arcs are rare objects so far observed. However, since our large area survey is very similar in sky area and depth to the *ROSAT* Deep Survey, and since both have produced a detection of a strong arc, the probability of detection seems high. Larger area surveys of X-ray selected clusters of galaxies with deep optical follow-up would help to determine the probability of detection. Such observations should put useful constraints on  $\Omega_m$  and on the density of galaxies at high redshifts (Cooray 1999).

It is interesting to note that all four of our clusters may have redshifts  $z \sim 0.4 - 0.5$  and are located within a region of only  $\sim 20'$  at the north-east corner of our field. This corresponds to a comoving radius of  $\sim 5$  Mpc. The implications of such large scale structure on the CXB need to be investigated further.

## 6. Summary

In this paper, we presented our CLASXS X-ray catalog. Our survey covers a  $\sim 0.4$  deg<sup>2</sup> contiguous area in an uniform manner and reaches fluxes of  $5 \times 10^{-16}$  ergs cm<sup>-2</sup> s<sup>-1</sup> in the 0.4–2 keV band and  $3 \times 10^{-15}$  ergs cm<sup>-2</sup> s<sup>-1</sup> in the 2–8 keV band. We found a total of 525 point sources and 4 extended sources. We summarize our results as follows.

1) The number counts in the 0.4–2 keV band agree very well with other large area surveys. On the other hand, the number counts in the 2–8 keV band deviate significantly from other large area surveys at the “knee” of the LogN-LogS, possibly as a result of the underlying large scale structure. The total 2–8 keV band flux agrees with the observed CXB flux within the observed variance of the CXB, indicating that the true normalization of the CXB can be determined using fields with solid angles  $\sim 0.3 - 0.4$  deg<sup>2</sup>.

- 2) The hardness ratios of the sources in the CLASXS field show a significant change at  $f_{2-8 \text{ keV}} \sim 10^{-14} \text{ ergs cm}^{-2} \text{ s}^{-1}$ , which bridges the range sampled by previous studies and confirms the results found in deep *Chandra/XMM-Newton* surveys. About 60% of the sources with full band fluxes  $> 4 \times 10^{-14}$  show significant variability, while the fraction drops dramatically with decreasing flux, at least partly due to selection effects. Most sources show no change of hardness ratio or anti-correlation with flux. But some sources show a positive correlation or mixed trends.
- 3) We report on the X-ray and multicolor analysis of four extended sources. We argue that the sources are likely low mass clusters or groups at redshifts  $\sim 0.5$ . Two of the clusters are probably interacting or merging.
- 4) We report on the discovery of a gravitational lensing arc. The lensing cluster is consistent with being at a redshift of  $z = 0.45 - 0.7$ .

We thank Dr. Jean Swank for the suggestion of C-statistics, Ann Harschemeier for discussions on *wavdetect*, and an anonymous referee for comments that helped to improve the paper. Y. Yang also thanks Dr. Chris Reynolds for his encouragement and help during this thesis work. This paper would not have been possible without the excellent work of the supporting staff at CXC and the superb instrument of the *Chandra X-ray Observatory*.

This project was partially funded under the IDS program of R. Mushotzky. We also gratefully acknowledge support from NASA's National Space Grant College and Fellowship Program and the Wisconsin Space Grant Consortium (A. T. S.), CXC grant GO2-3191A (A. J. B.), NSF grants AST-0084847 and AST-0239425 (A. J. B.) and AST-0084816 (L. L. C.), and the University of Wisconsin Research Committee with funds granted by the Wisconsin Alumni Research Foundation, the Alfred P. Sloan Foundation, and the David and Lucile Packard Foundation (A. J. B.). This paper is part of Y. Yang's PhD thesis work at the University of Maryland.

## REFERENCES

- Akiyama, M., Ueda, Y., Ohta, K., Takahashi, T., & Yamada, T. 2003, *ApJS*, 148, 275
- Alexander, D. M., Brandt, W. N., Hornschemeier, A. E., Garmire, G. P., Schneider, D. P., Bauer, F. E., & Griffiths, R. E. 2001, *AJ*, 122, 2156
- Alexander, D. M., et al. 2003, *AJ*, 126, 539
- Baldi, A., Molendi, S., Comastri, A., Fiore, F., Matt, G., & Vignali, C. 2002, *ApJ*, 564, 190
- Barger, A. J., Cowie, L. L., Mushotzky, R. F., & Richards, E. A. 2001, *AJ*, 121, 662
- Barger, A. J., et al. 2003, *AJ*, 126, 632
- Barr, P. 1986, *MNRAS*, 223, 29
- Bauer, F. E., et al. 2002, *AJ*, 123, 1163

- Brandt, W. N., et al. 2001, *AJ*, 122, 2810
- Bolzonella, M., Miralles, J.-M., & Pelló, R. 2000, *A&A*, 363, 476
- Cash, W. 1979, *ApJ*, 228, 939
- Cooray, A. R. 1999, *ApJ*, 524, 504
- Cowie, L. L., Garmire, G. P., Bautz, M. W., Barger, A. J., Brandt, W. N., & Hornschemeier, A. E. 2002, *ApJ*, 566, L5
- Dickey, J. M., & Lockman, F. J. 1990, *ARA&A*, 28, 215
- Ettori, S., Tozzi, P., & Rosati, P. 2003, *A&A*, 398, 879
- Freeman, P. E., Kashyap, V., Rosner, R., & Lamb, D. Q. 2002, *ApJS*, 138, 185
- Finoguenov, A., Reiprich, T. H., & Böhringer, H. 2001, *A&A*, 368, 749
- Gehrels, N. 1986, *ApJ*, 303, 336
- Giacconi, R., et al. 2002, *ApJS*, 139, 369
- Gladders, M. D. & Yee, H. K. C. 2000, *AJ*, 120, 2148
- Harrison, F. A., Eckart, M. E., Mao, P. H., Helfand, D. J., & Stern, D. 2003, *ApJ*, 596, 944
- Hasinger, G. 2003, in “The Restless High Energy Universe”, Eds. E. P. J. van den Heuvel, J.J.M. in ’t Zand, & R.A.M.J. Wijers, *Nucl. Physics B. Suppl. Ser.*, in press (astro-ph/0310804)
- Hasinger, G., et al. 1998b, *A&A*, 340, L27
- Humason, M. L., Mayall, N. U., & Sandage, A. R. 1956, *AJ*, 61, 97
- Kawara, K., et al. 2004, *A&A*, 413, 843
- Kim, D.-W., et al. 2004, *ApJS*, 150, 19
- Kushino, A., Ishisaki, Y., Morita, U., Yamasaki, N. Y., Ishida, M., Ohashi, T., & Ueda, Y. 2002, *PASJ*, 54, 327
- Moretti, A., Campana, S., Lazzati, D., & Tagliaferri, G. 2003, *ApJ*, 588, 696
- Mushotzky, R. F., Figueroa-Feliciano, E., Loewenstein, M., & Snowden, S. L. 2003 (astro-ph/0302267)
- Mushotzky, R. F., Cowie, L. L., Barger, A. J., & Arnaud, K. A. 2000, *Nature*, 404, 459
- Nandra, K., George, I. M., Mushotzky, R. F., Turner, T. J., & Yaqoob, T. 1997, *ApJ*, 476, 70
- Piconcelli, E., Cappi, M., Bassani, L., Fiore, F., Di Cocco, G., & Stephen, J. B. 2002, *A&A*, 394, 835
- Piconcelli, E., Cappi, M., Bassani, L., Di Cocco, G., & Dadina, M. 2003, *A&A*, 412, 689
- Postman, M., & Lauer T. 1995, *ApJ*, 440, 28
- Revnivtsev, M., Gilfanov, M., Sunyaev, R., Jahoda, K., & Markwardt, C. 2003, *A&A*, 411, 329
- Schmidt M., et al. 1998, *A&A*, 329, 495

Tozzi, P., et al. 2001, ApJ, 562, 42

Vikhlinin, A., Forman, W., Jones, C., & Murray, S. 1995, ApJ, 451, 542

Yang, Y., Mushotzky, R. F., Barger, A. J., Cowie, L. L., Sanders, D. B., & Steffen, A. T. 2003, ApJ, 585, L85

Yee, H. K. C., & Gladders, M. D. 2002, in “AMiBA 2001: High-Z Clusters, Missing Baryons, and CMB Polarization”, Eds. L.-W. Chen, C.-P. Ma, K.-W. Ng, & U.-L. Pen, (San Francisco: ASP Conference Series), p109 (astro-ph/0111431)

Table 1. Observation Summary

Target Name	$\alpha_{2000}$	$\delta_{2000}$	Obs ID	Sequence #	Observation date	Exposure <sup>a</sup>
LHNW1	10 34 00.24	+57 46 10.6	1698	900057	05/17/01 18:29:38	72.97 ks
LHNW2	10 33 19.82	+57 37 13.8	1699	900058	04/30/01 10:59:38	40.74 ks
LHNW3	10 34 36.12	+57 37 10.9	1697	900056	05/16/01 12:46:50	43.72 ks
LHNW4	10 32 04.20	+57 37 15.6	3345	900184	04/29/02 03:23:45	38.47 ks
LHNW5	10 34 00.31	+57 28 15.6	3346	900185	04/30/02 02:03:59	38.21 ks
LHNW6	10 33 20.28	+57 55 15.2	3343	900182	05/03/02 09:11:41	34.04 ks
LHNW7	10 32 44.23	+57 46 15.2	3344	900183	05/01/02 20:03:06	38.54 ks
LHNW8	10 34 36.26	+57 55 15.6	3347	900186	05/02/02 14:16:27	38.46 ks
LHNW9	10 35 14.28	+57 46 15.2	3348	900187	05/04/02 11:01:47	39.52 ks

<sup>a</sup>Total good time with dead time correction.

Table 3. Extended Sources

Source #	$\alpha_{2000}$	$\delta_{2000}$	$\Delta\alpha$ (")	$\Delta\delta$ (")	$\theta$ (') <sup>a</sup>	PSF ratio <sup>b</sup>	Net Counts <sup>c</sup>	Field <sup>d</sup>
1	10 35 25.4	+57 50 48	2.628	1.044	4.786	37.89	100.1 ± 11	9
2	10 35 13.4	+57 50 17	3.312	1.476	4.029	39.33	87.7 ± 11	9
3	10 35 37.9	+57 57 15	3.060	1.476	8.422	19.09	77.0 ± 10	8
4	10 34 30.8	+57 59 12	3.132	2.196	4.016	16.69	30.7 ± 6.6	8

<sup>a</sup>Off-axis angle in the field the source is detected.

<sup>b</sup>Defined as  $\sqrt{(A/\pi)}/r_{99}$ , where  $A$  is the area of the source region from the *vtpdetect* report and  $r_{99}$  is the 99% PSF radius at the off-axis angle.

<sup>c</sup>Net counts reported by *vtpdetect*

<sup>d</sup>LHNW field number where the source has the smallest off-axis angle.

Table 4. Redshift estimates for the extended Sources

Source #	$z_{RS}$	$z_{BCG}$	$z_{X-ray}$
1	0.50	0.58 <sup>+0.08</sup> <sub>-0.08</sub>	0.5 ± 0.2
2	0.50	0.73 <sup>+0.09</sup> <sub>-0.08</sub>	0.5 ± 0.2
3	.....	0.73 <sup>+0.09</sup> <sub>-0.08</sub>	.....
4	0.45	0.45 <sup>+0.06</sup> <sub>-0.05</sub>	.....

Table 5. Properties of the extended sources

Source #	$z_{fix}$	kT <sup>a</sup>	$M_{500}$ <sup>b</sup>	core radius (")	$f_{0.5-8keV}$ <sup>c</sup>	$L_{bol}$ <sup>d</sup>
1	.50	1.4 <sup>+0.8</sup> <sub>-0.4</sub>	0.45 <sup>+0.61</sup> <sub>-.21</sub>	12.9	1.6	2.2
2	.50	3.1 <sup>+6.5</sup> <sub>-1.4</sub>	2.0 <sup>+15.</sup> <sub>-1.4</sub>	17.0	1.2	1.5
3	.73	2.3 <sup>+1.0</sup> <sub>-0.9</sub>	1.2 <sup>+1.2</sup> <sub>-.64</sub>	14.7	1.5	5.1
4	.45	1.0 (fixed)	.24	11.8	.42	.45

<sup>a</sup>Listed are single parameter  $1\sigma$  errors.

<sup>b</sup>unit:  $10^{14} M_{\odot}$

<sup>c</sup>Unit:  $10^{-14} \text{ ergs cm}^{-2} \text{ s}^{-1}$ .

<sup>d</sup>Unit:  $10^{43} \text{ ergs s}^{-1}$ .

Fig. 1.— Layout of the 9 ACIS-I pointings. Gray scale map shows the adaptively smoothed full band image. The exposure maps are added (light gray) to outline the ACIS-I fields. Fields are separated by  $10'$  from each other. The field numbers (LHNW1-9) are shown at the center of each ACIS-I field.

Fig. 2.— Offset between the corrected X-ray positions and the optical positions. The  $135^\circ$  and  $45^\circ$ , as measured from positive x-axis, shaded histogram represents sources with best positions within  $4'$  and between  $4'$  and  $6'$  of the optical axis, respectively. The unshaded histogram shows the sources with off-axis angles  $> 6'$ .

Fig. 3.— Broadband PSFs obtained from our observations (*solid lines*) compared with the monochromatic PSFs from the PSF library (*dashed lines*). Both the observed broadband PSFs and the monochromatic PSFs are normalized to the wing. From the narrowest to the broadest, each broadband PSF is constructed within each of the off-axis angle intervals  $0'-4'$ ,  $4'-6'$ ,  $6'-7'$ ,  $7'-8'$ ,  $8'-9'$ ,  $9'-12'$ . The library PSFs are taken at the midpoints of these off-axis intervals. (a) Soft band PSF vs. 0.91 keV library PSF; (b) hard band PSF vs. 4.2 keV library PSF.

Fig. 4.— Examples of the source and background regions used in the flux extraction. The smaller circle is the source region. The background regions are shown as segments of an annulus. Segments with counts below  $3\sigma$  of the mean are used in the final background estimation and are marked with 'X' symbols. (a) An isolated source; (b) a source with a close neighbor.

Fig. 5.— Comparison of net counts from *wavdetect* and our aperture photometry (marked as XPHOTO) for the (a) soft, (b) hard, and (c) full bands.

Fig. 6.— Distribution of off-axis angles of the best positions.

Fig. 7.— Distribution of multiple detections.

Fig. 8.— Thresholds for 95% completeness vs. off-axis angle. Sources with flux and off-axis angle combinations above these curves are complete. Solid, dashed, and dotted lines represent the threshold curves for the soft, hard, and full bands, respectively. Squares represent the 70 ks exposure and diamonds the 40 ks exposure.

Fig. 9.— Survey effective solid angle vs. flux. Soft band (*solid line*); full band (*dashed line*); hard band (*dotted line*).

Fig. 10.— Average output fluxes from *wavdetect* vs. average input fluxes for the simulated sources at a set of off-axis angles (*diamonds*). The Eddington bias is seen in the overestimates of output flux at low fluxes. The bias also increases at large off-axis angles. The best fit of the biases are shown as dotted lines for off-axis angle intervals  $0'-2.5'$ ,  $2.5'-4'$ ,  $4'-6'$ ,  $6'-8'$ , and  $> 8'$ .

Fig. 11.— Cumulative LogN-LogS for the soft and hard bands. The  $1\sigma$  error is shaded. Dash-dotted line represents the best fit from Moretti et al. (2003). Hard band LogN-LogS from Moretti

et al. is rescaled to that of 2 – 8 keV, assuming  $\Gamma = 1.4$ .

Fig. 12.— Differential LogN-LogS for the soft and hard bands. The unit of  $dN/dS$  is number per  $10^{-15} \text{ ergs cm}^{-2} \text{ s}^{-1}$ . Best-fit power laws are shown as solid lines. Dotted line represents a power law with a fixed index of  $-2.5$ . The data do not constrain the slope at high fluxes well. Dashed line shows the best fit of the hard band LogN-LogS from the SEXSI survey (Harrison et al. 2003) and the dash-dotted line is the best fit from Cowie et al. (2002).

Fig. 13.— Hardness ratio vs. full band flux for the CLASXS sources. Open circles with arrows represent the upper or lower limits. Dashed lines with numbers label the hypothetical spectral indices, assuming the source spectra are single power laws with only Galactic absorption. Dotted line represents the typical error size of the hardness ratio for a source with hardness ratio of 1.

Fig. 14.— Hardness ratio of the stacked sources in different flux bins. Crosses are the CLASXS sources and diamonds are the combined CDFs sources (Alexander et al. 2003). Sources with fluxes below  $8 \times 10^{-15} \text{ ergs cm}^{-2} \text{ s}^{-1}$  in the CLASXS catalog and  $1 \times 10^{-15} \text{ ergs cm}^{-2} \text{ s}^{-1}$  in the CDFs catalogs are not included to avoid incompleteness. Dashed lines are as in Figure 10.

Fig. 15.— Light curves of the sources detected to be variable. The fluxes are normalized to the mean of all the observations. Numbers in the plots are the source numbers in the catalog. (a) Soft band; (b) hard band; (c) full band.

Fig. 16.— (*Upper panel*) Fraction of sources that are variable in different flux bins. (*Lower panel*) Number of variable sources (*dashed histogram*) and total number of sources tested for variability (*solid histogram*) in the same flux bins as in the upper panel.

Fig. 17.— Excess variability for the variable sources in each energy band vs. the flux of that band. (a) Soft band; (b) hard band; (c) full band.

Fig. 18.— Spectral variability vs. full band fluxes for all the variable sources. The fluxes are in units of  $10^{-14} \text{ ergs cm}^{-2} \text{ s}^{-1}$ . Numbers on top of each plot are the source numbers in the catalog.

Fig. 19.— Adaptively smoothed X-ray images of the extended sources superposed on R band images. (a) Sources 1 and 2; (b) Source 3; (c) Source 4.

Fig. 20.— Regions for spectral extraction of Sources 1 and 2 on the Gaussian smoothed gray scale map of the clusters. The Gaussian kernel size is  $6''$ . Source regions are shown as circles. Elliptical annulus region is for the background extraction.

Fig. 21.— X-ray spectra and best-fit MEKAL models of Source 1 (*dash-dotted line*) and Source 2 (*solid line*).

Fig. 22.— Combined probability contour of the temperature of Sources 1 and 2. Contour lines are 1, 2, and  $3\sigma$  confidence levels. Cross is the best-fit temperature. Solid line represents the equality

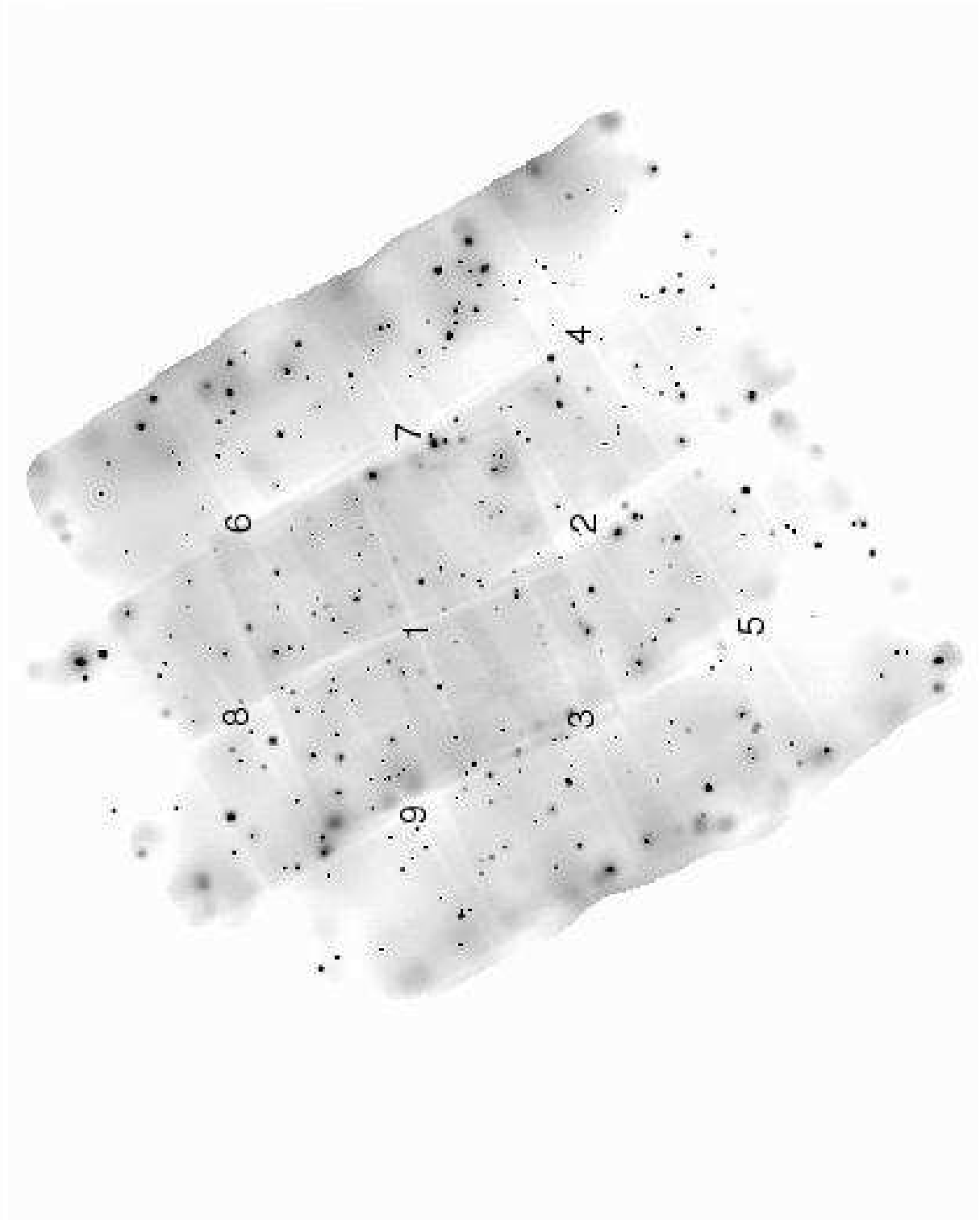
of the temperature of the two clusters.

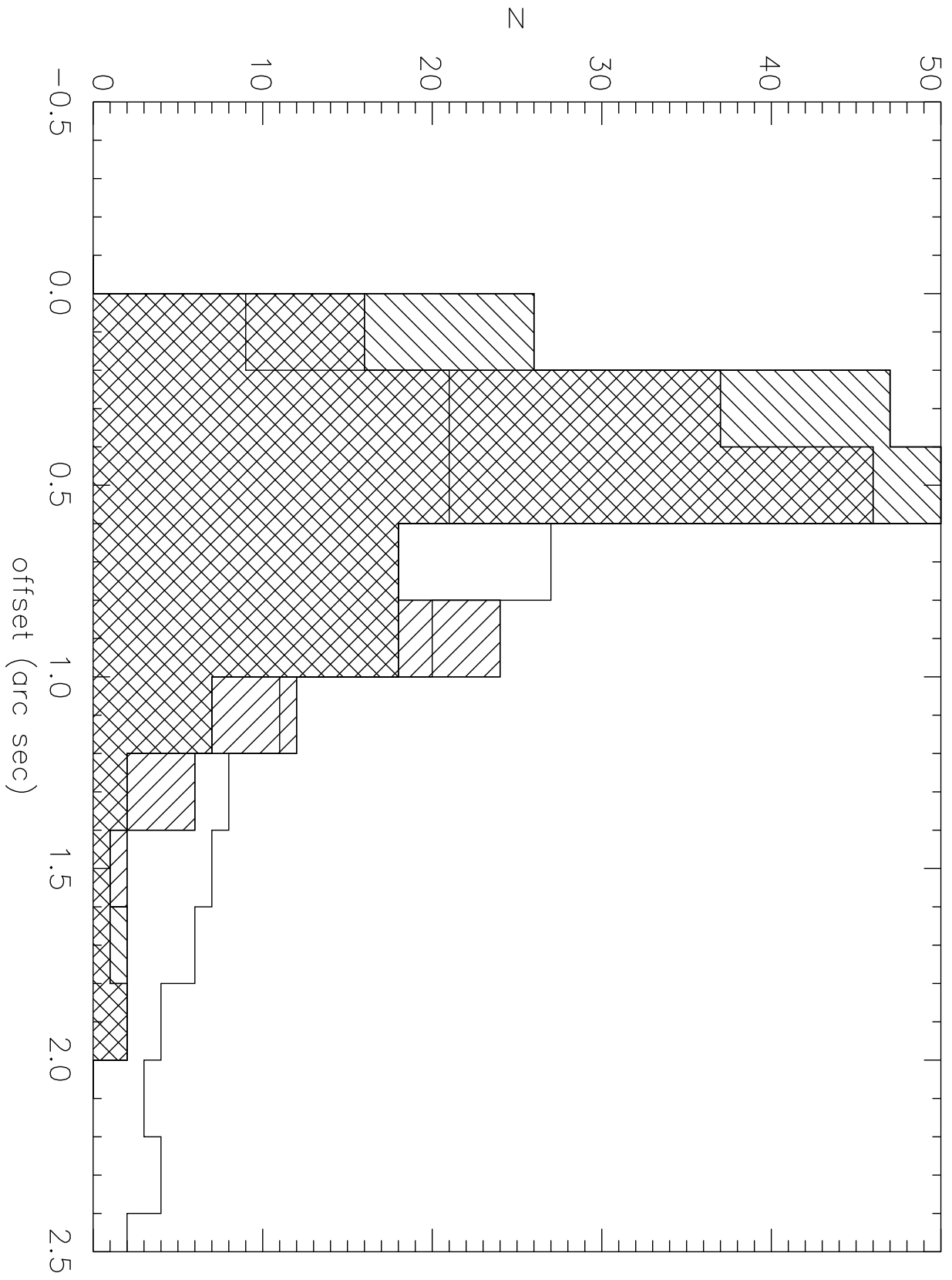
Fig. 23.— X-ray spectrum of Source 3 and the best-fit MEKAL model.

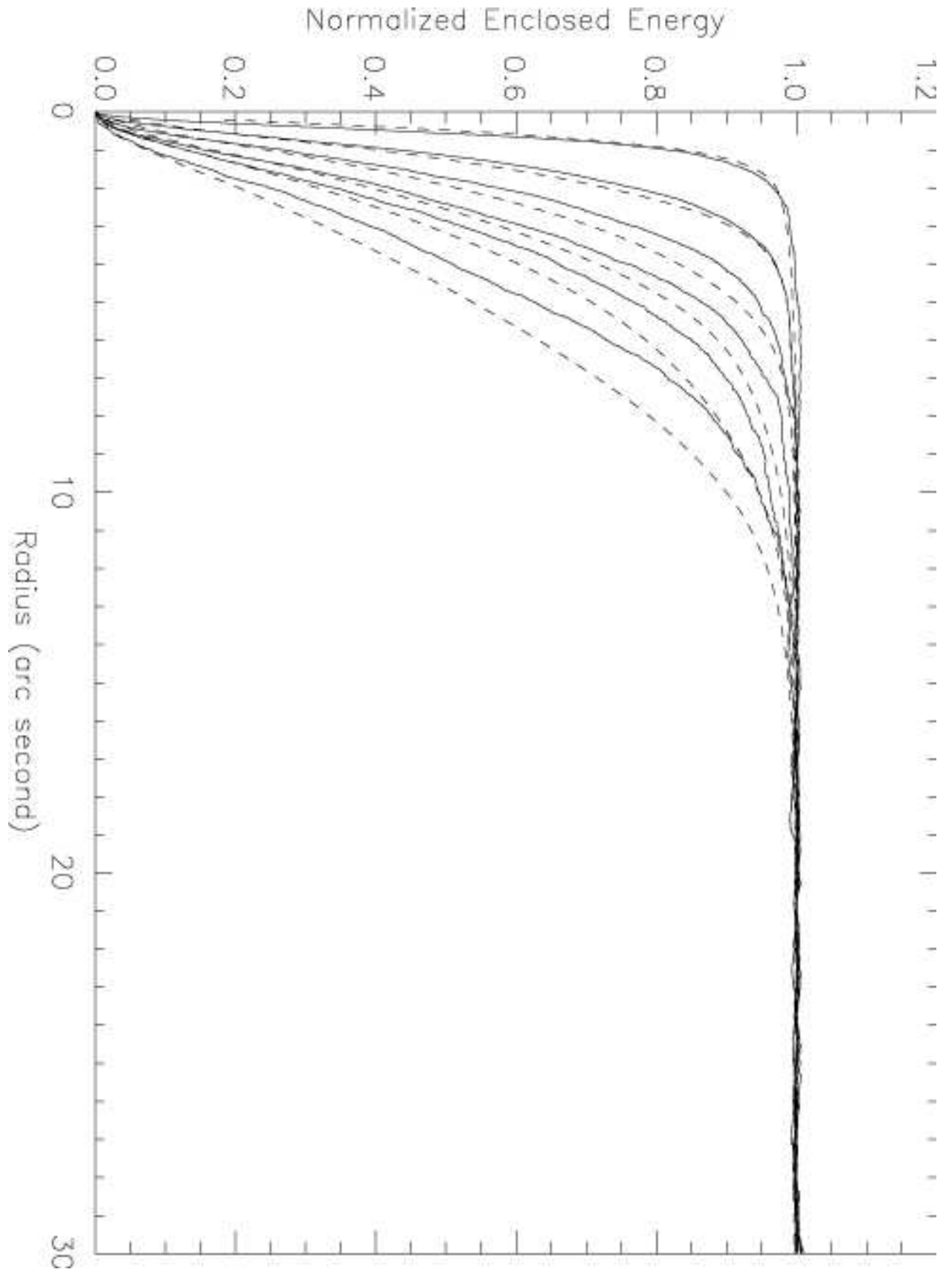
Fig. 24.— Curve-of-growths for the extended sources (Sources 1 – 4 shown in pannels (a) –(d)) normalized to the best-fit background. Dotted line shows the best fit of an integrated 2 dimensional Gaussian.

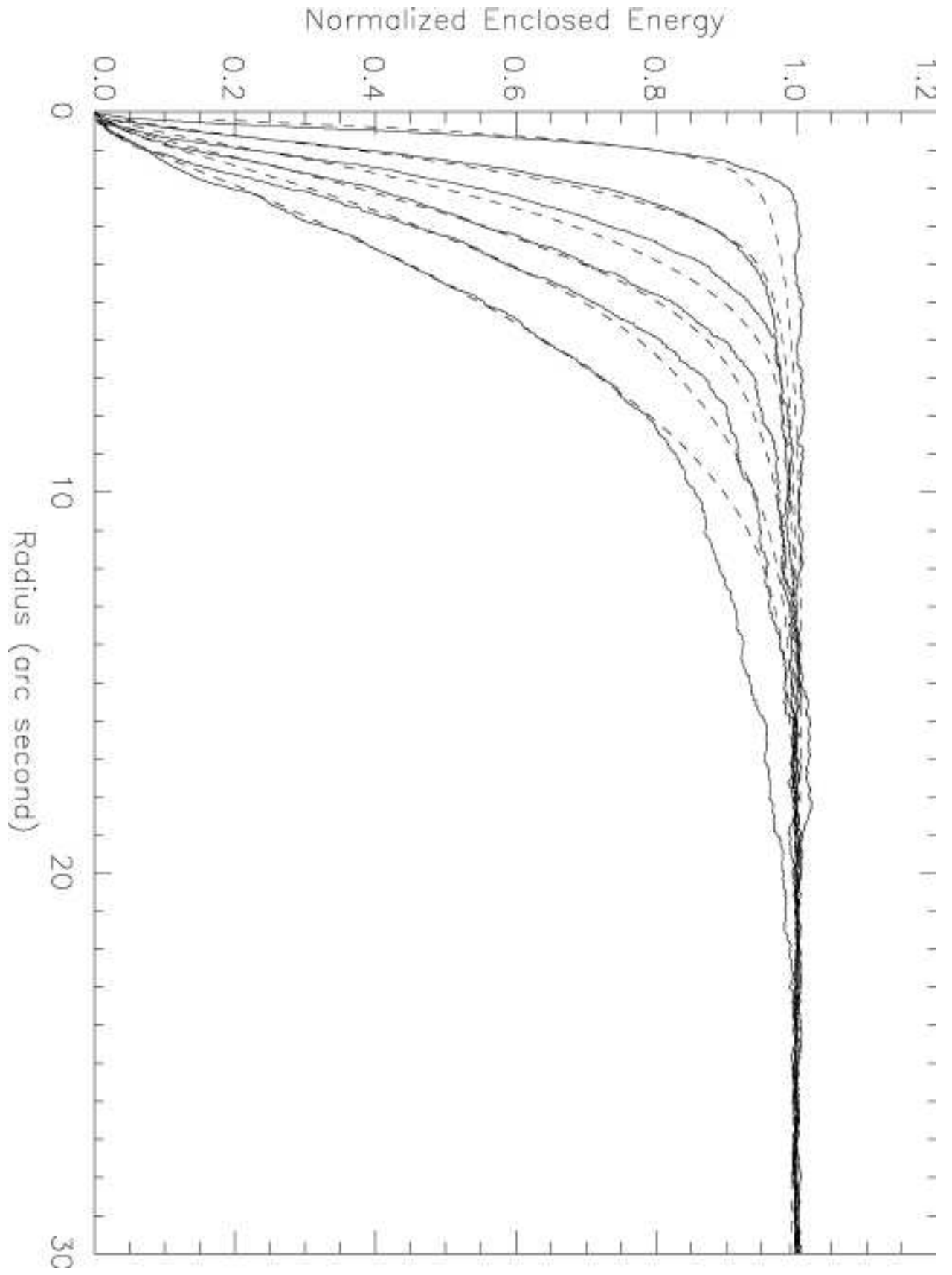
Fig. 25.— Color-magnitude plot for the galaxies within  $0.5'$  of the X-ray center. Solid lines show the model red sequence from Yee & Gladders (2001) at the redshifts that best match the observations in Source 1 ( $z = 0.5$ ), 2 ( $z = 0.5$ ), and 4 ( $z = 0.45$ ). In the plot for Source 4, the red sequences for  $z = 0.5$  (lower solid line) and  $z = 1.0$  (upper solid line) are shown.

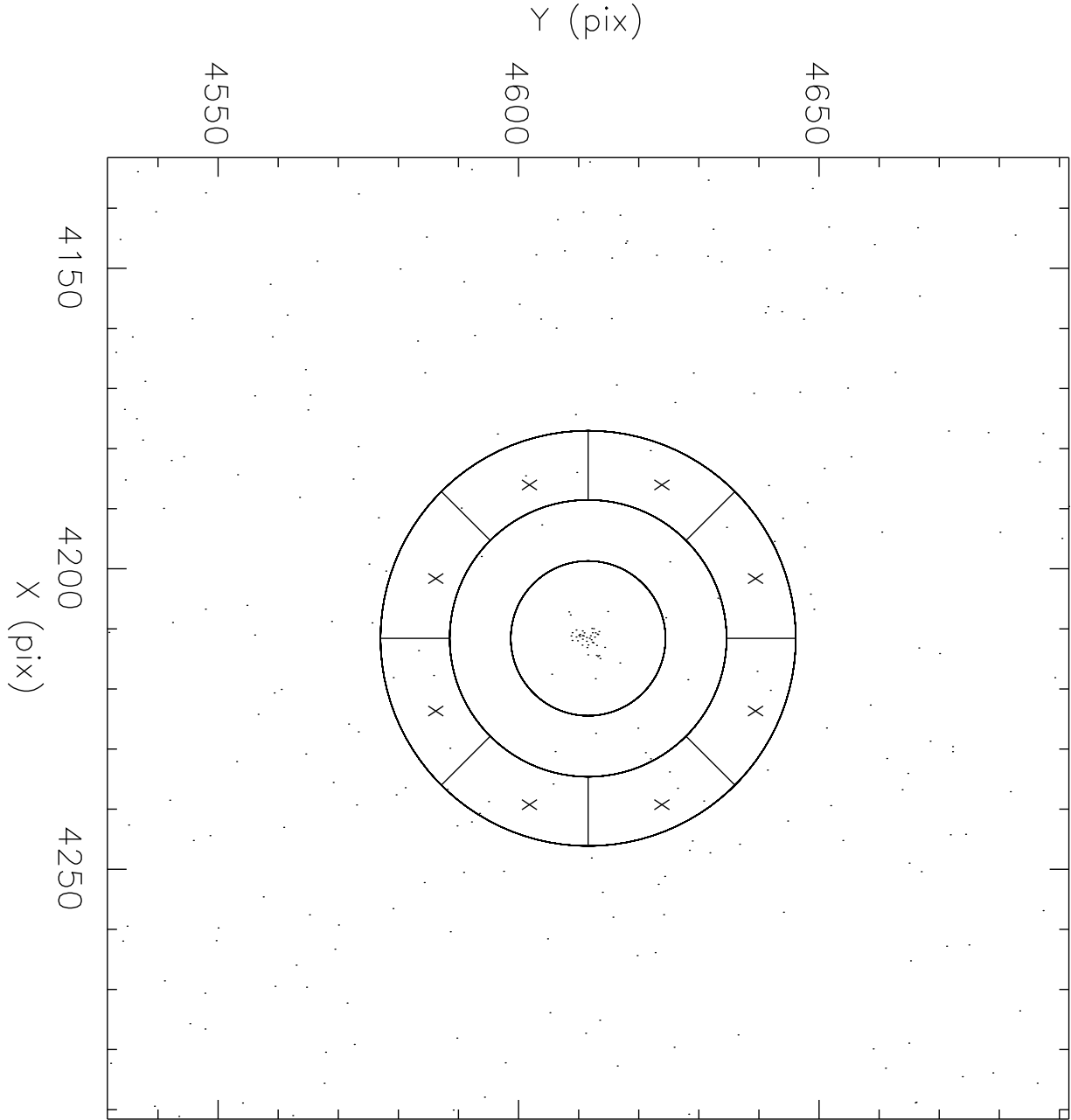
Fig. 26.—  $R$  band image of the gravitational lensing arc found associated with Source 3.

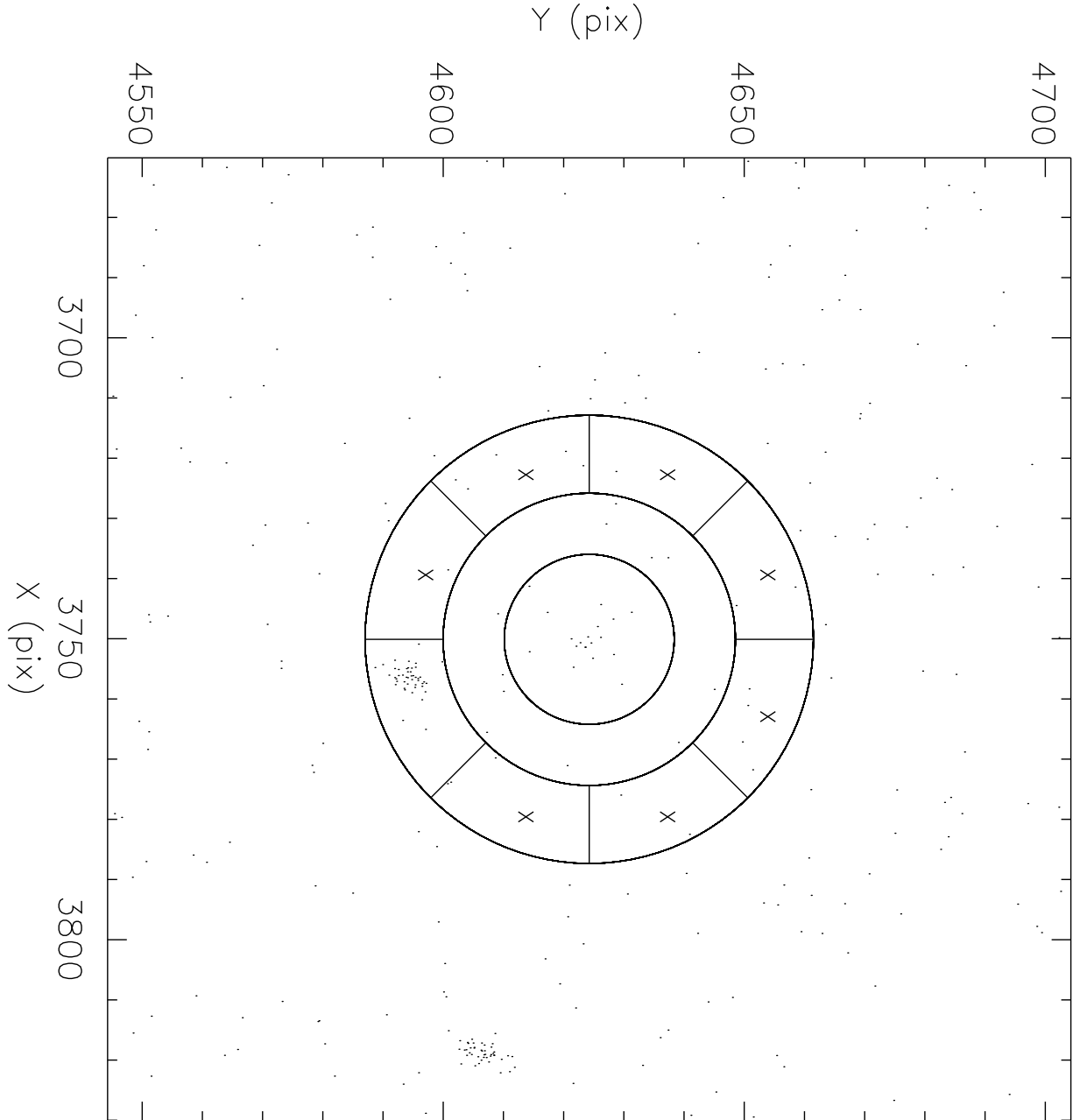


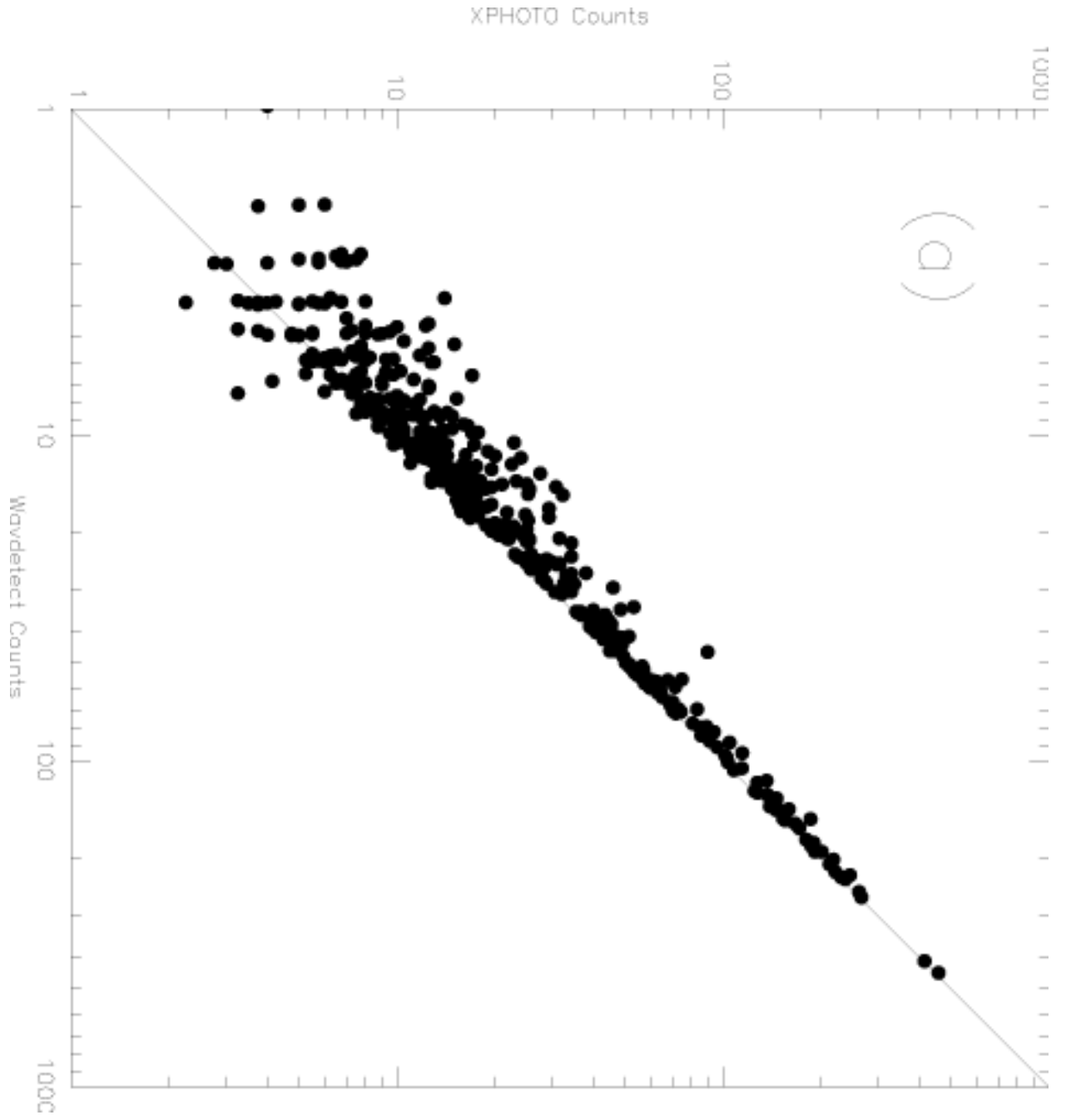


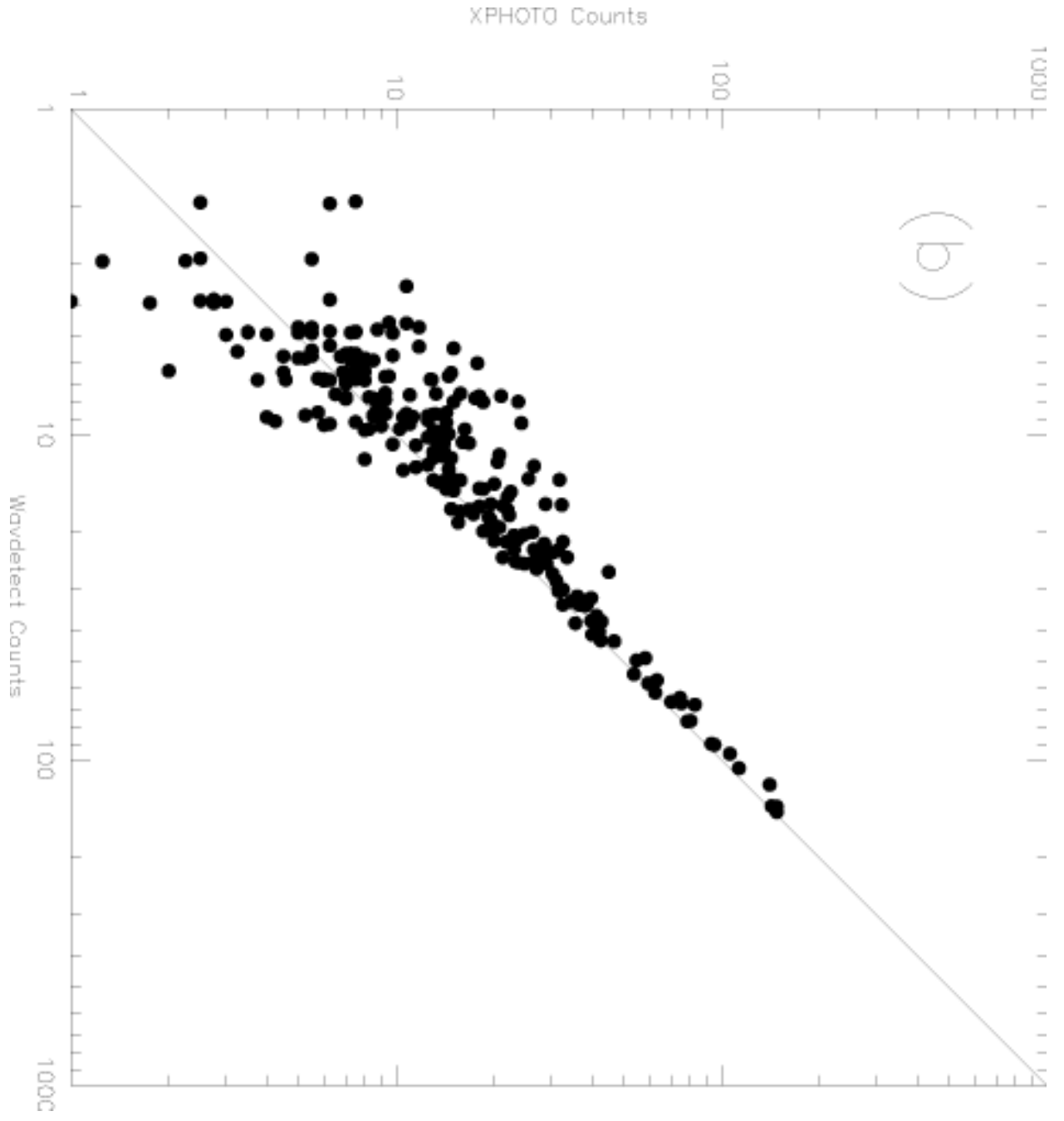


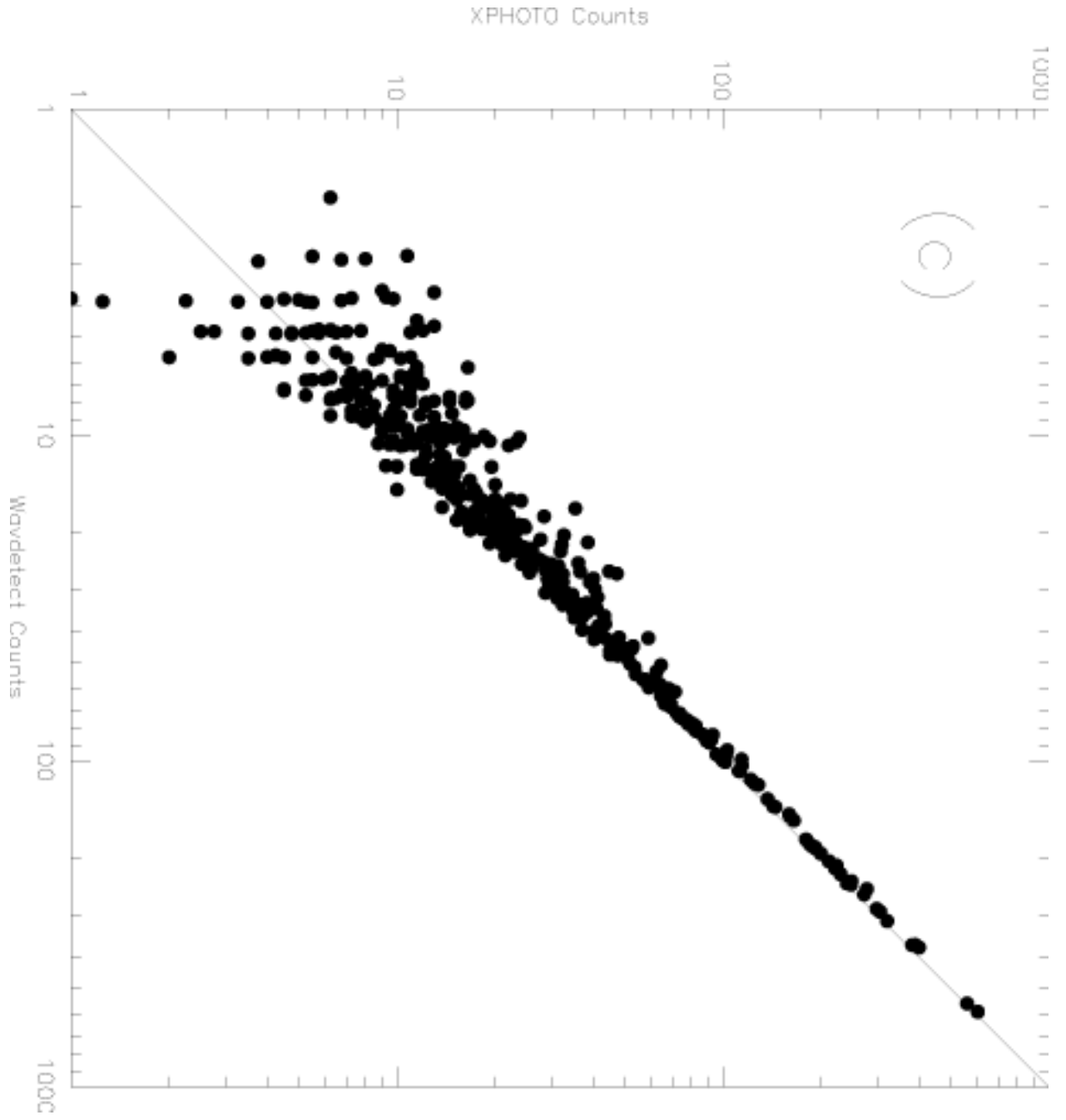


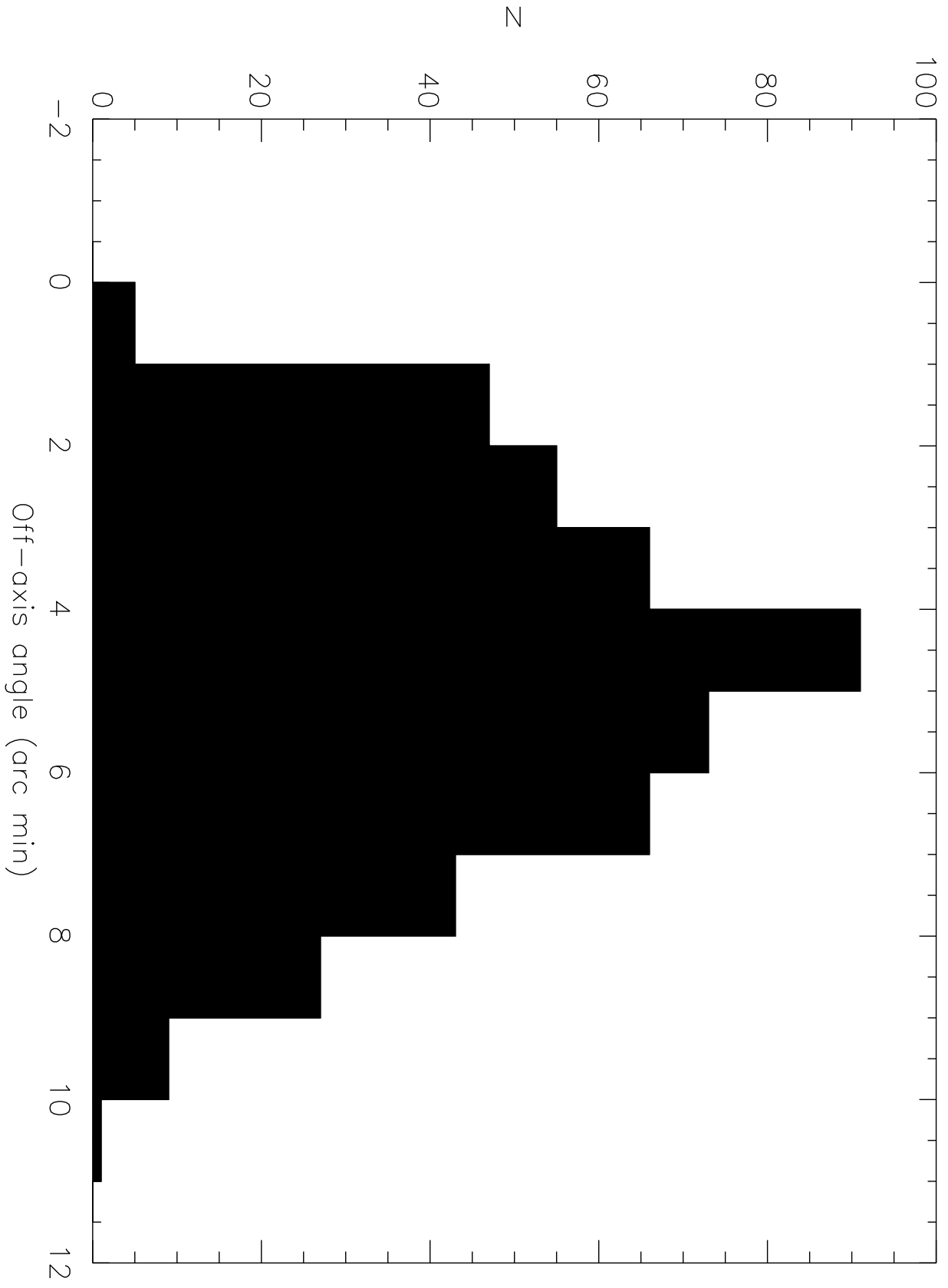


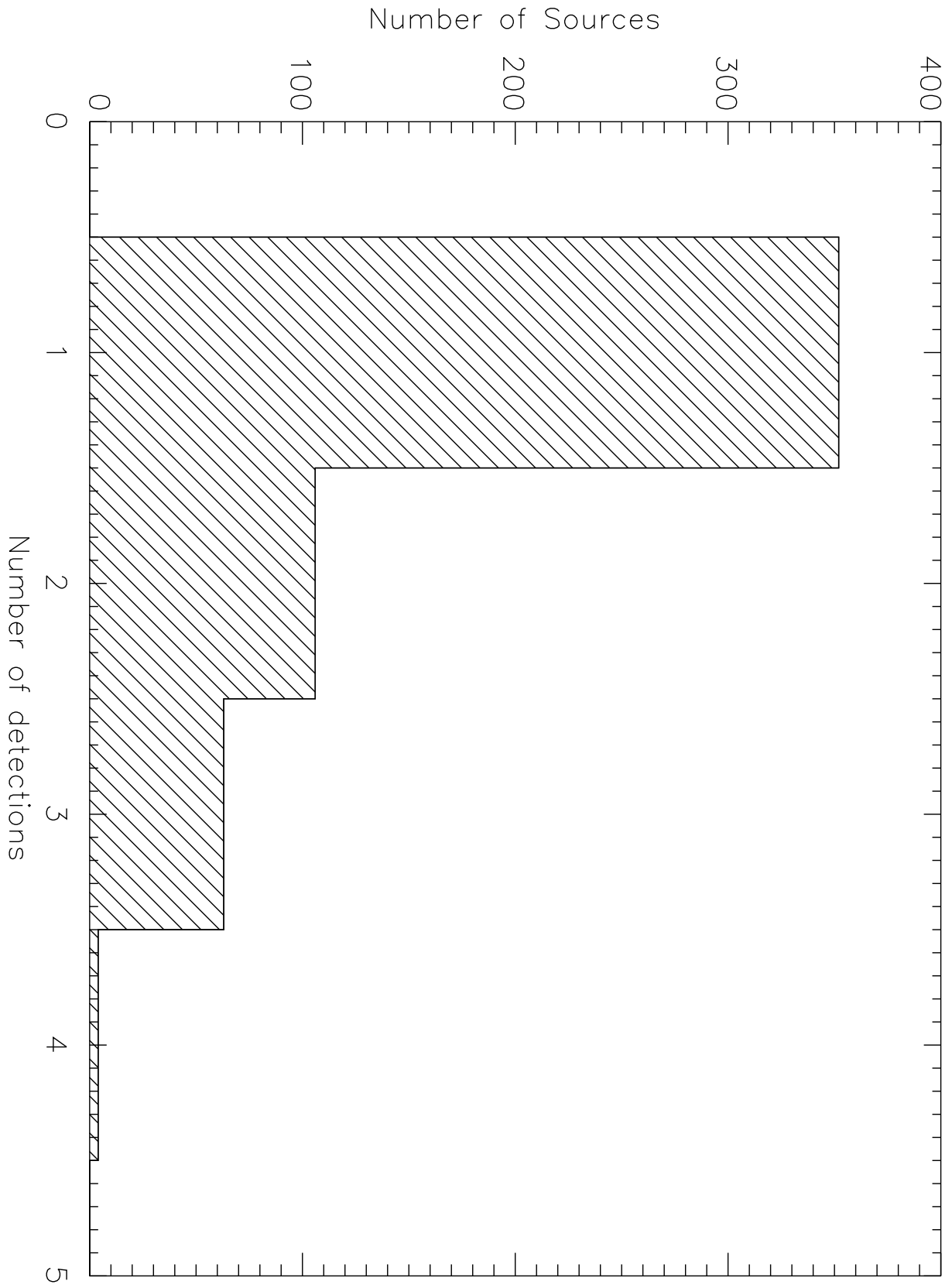




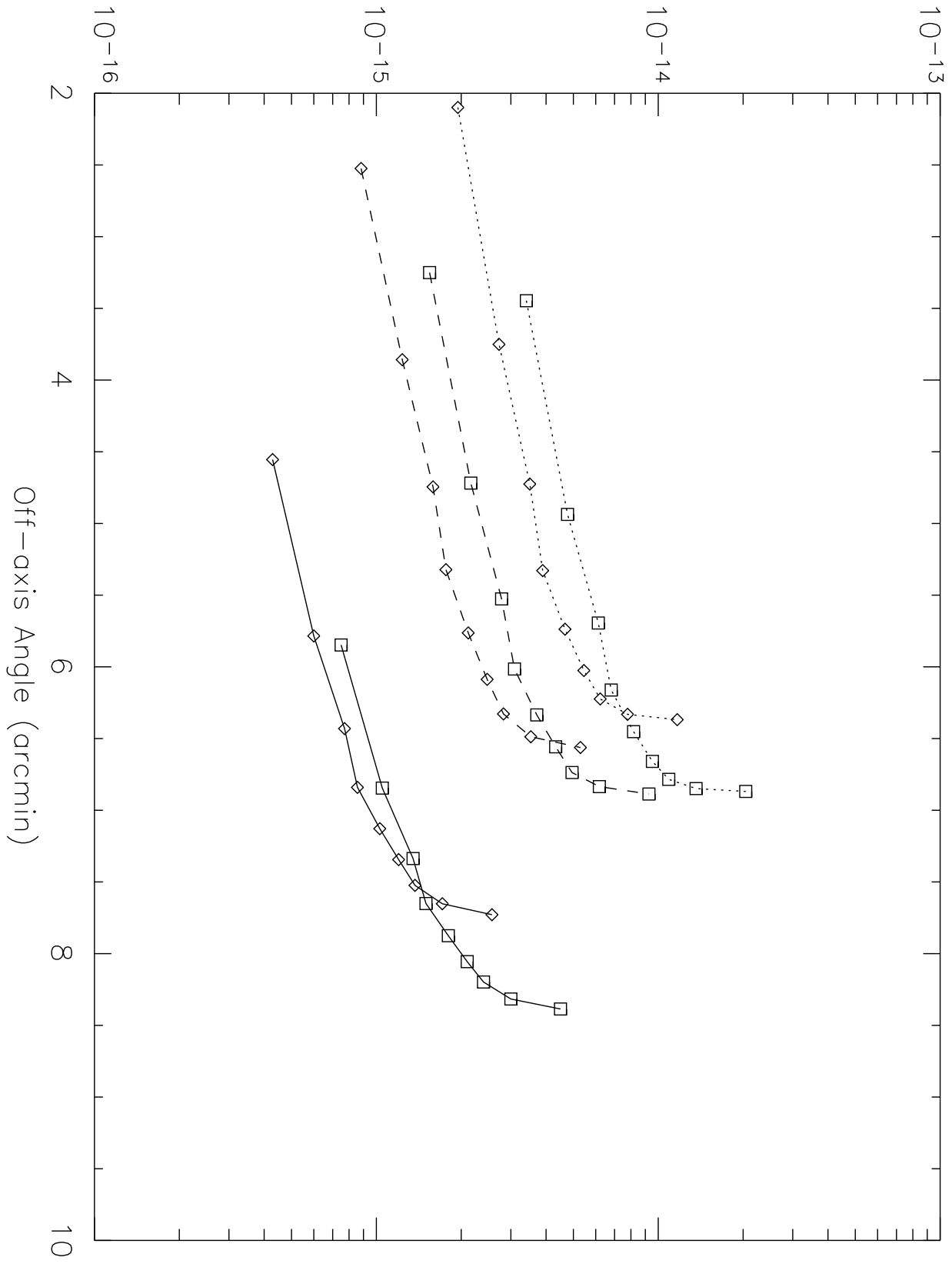


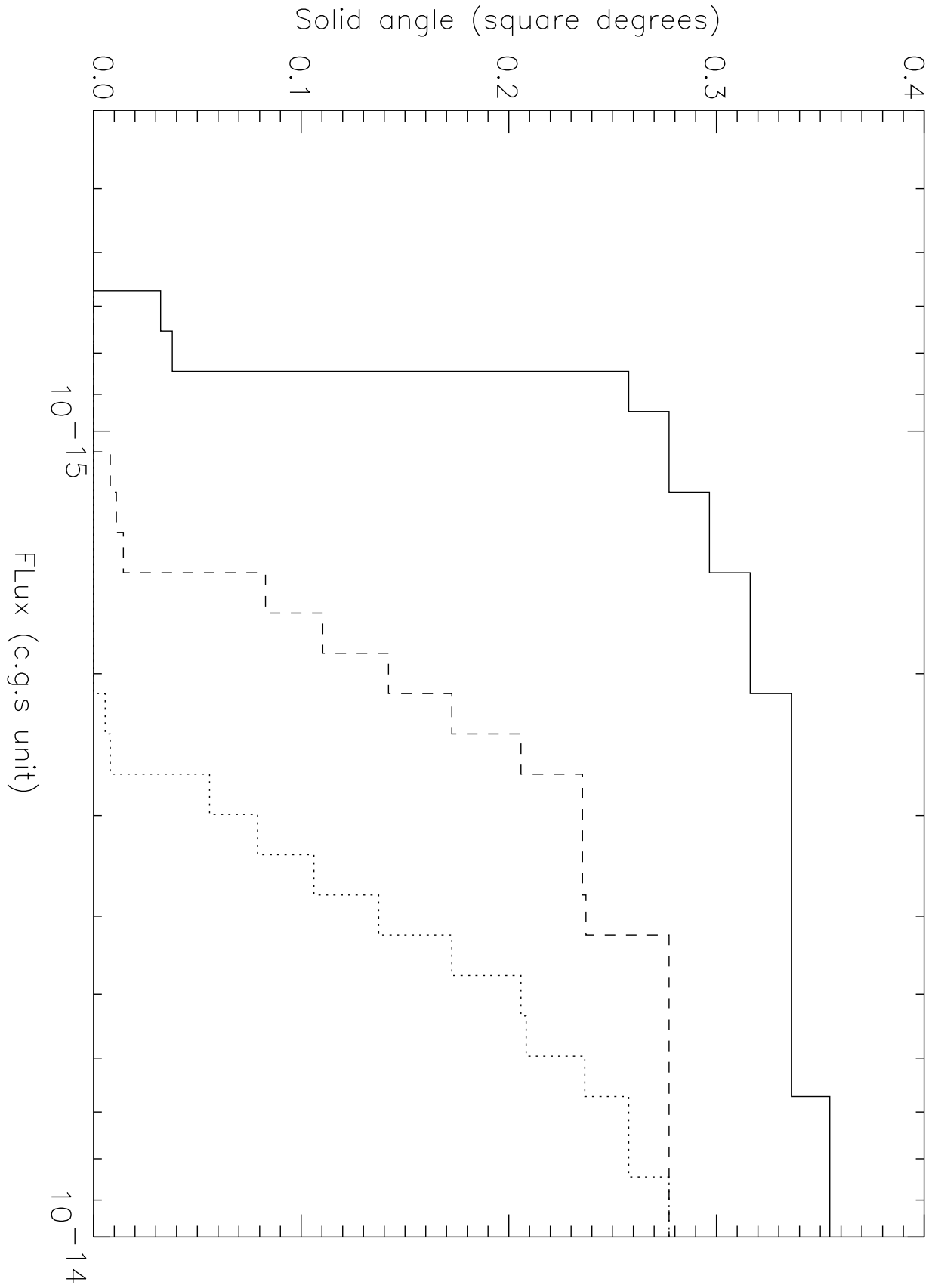


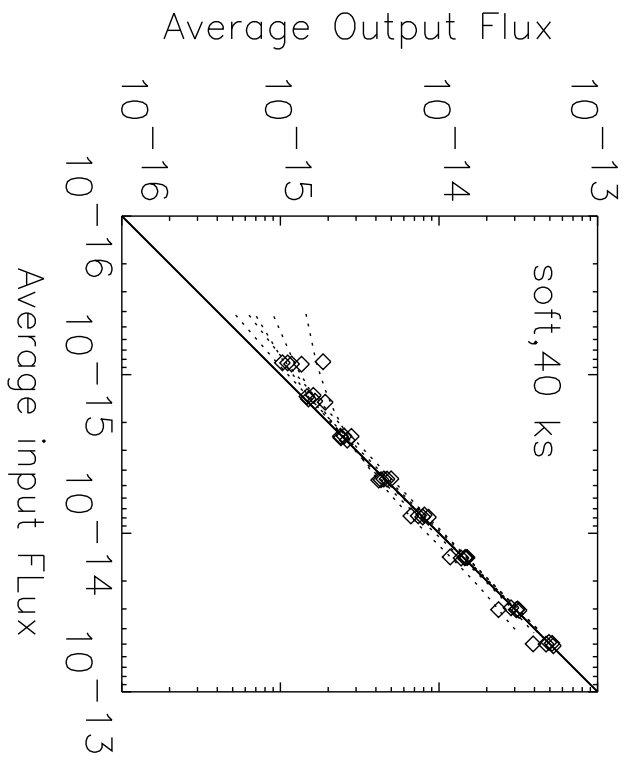
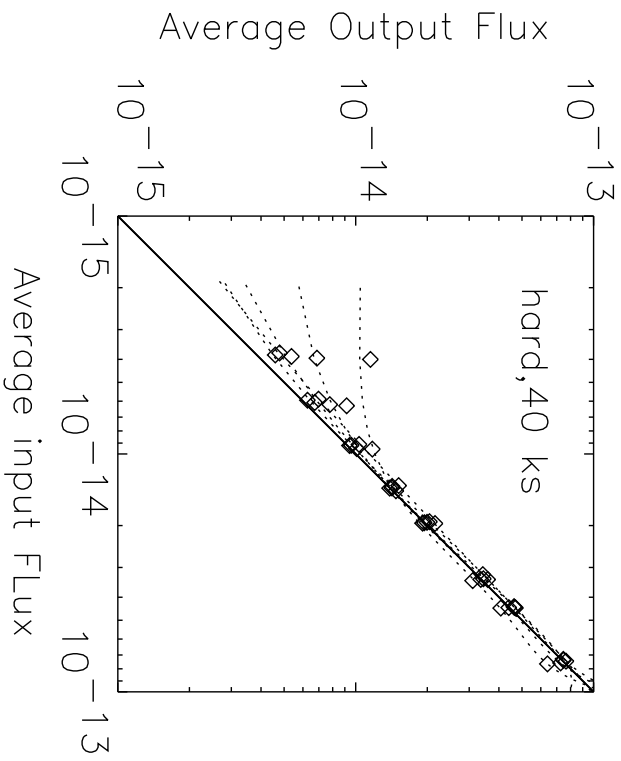
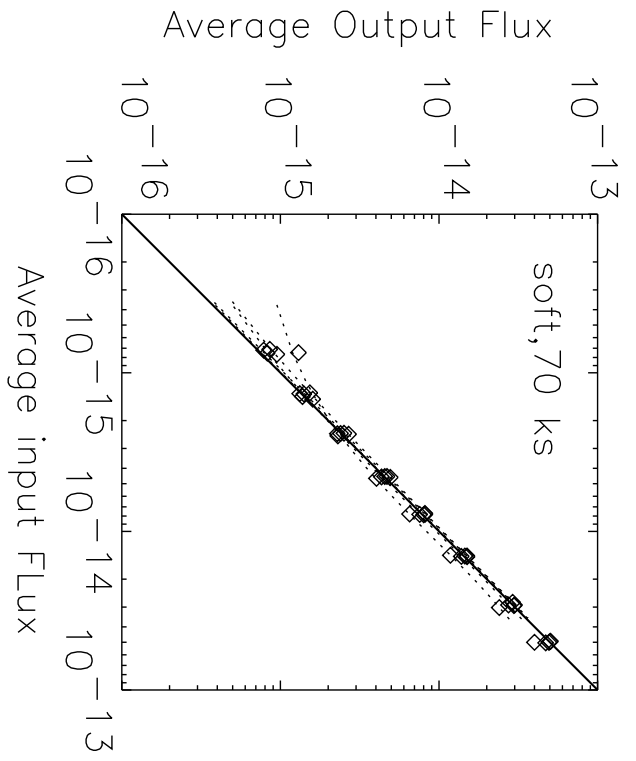
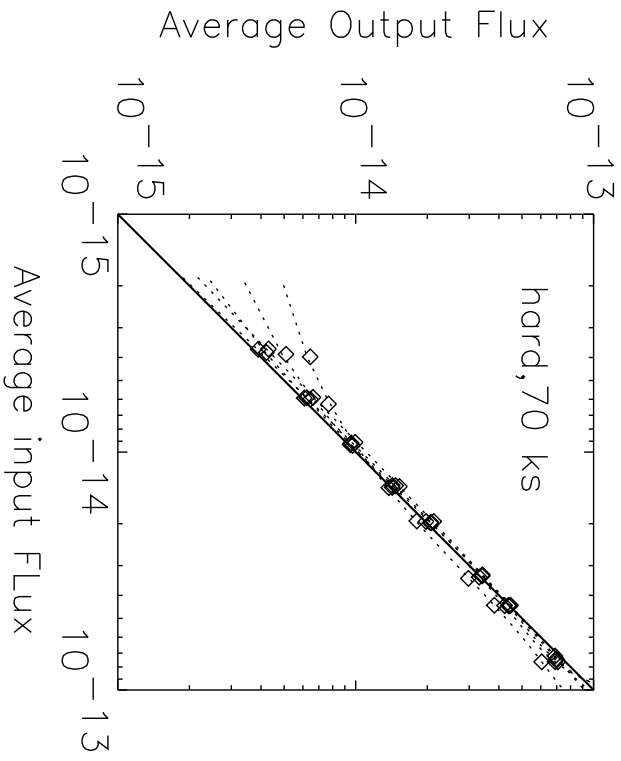


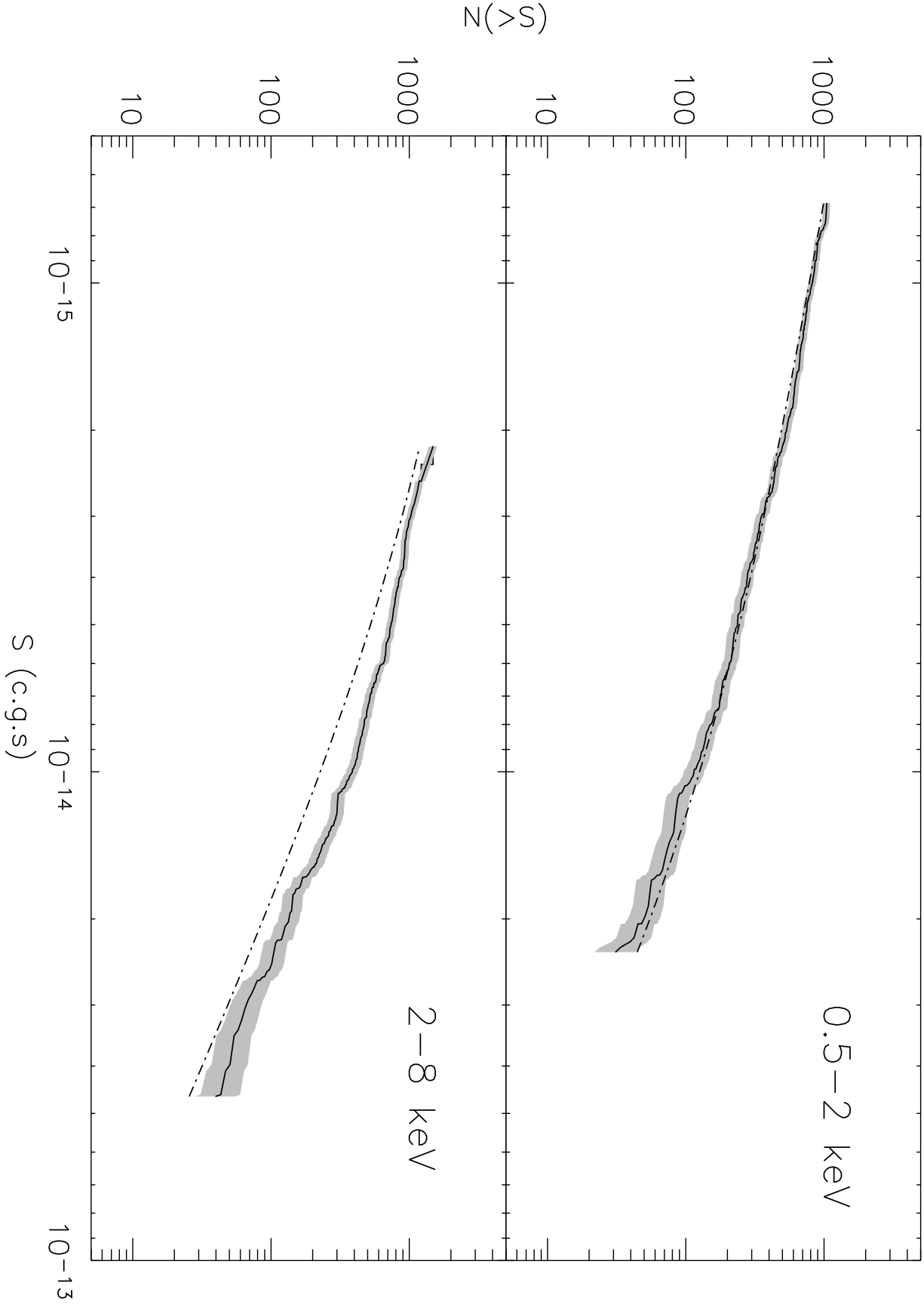


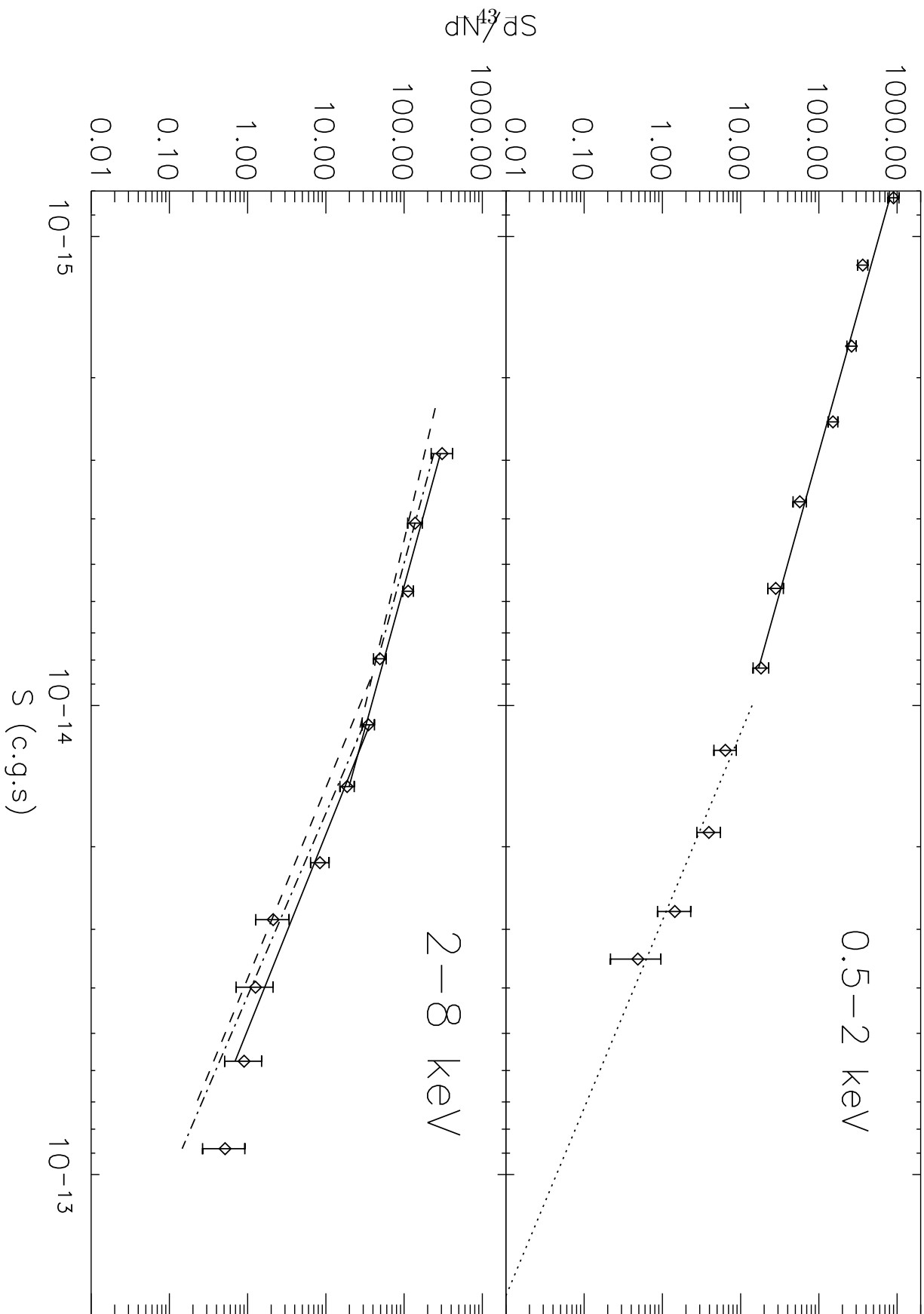
Flux Threshold

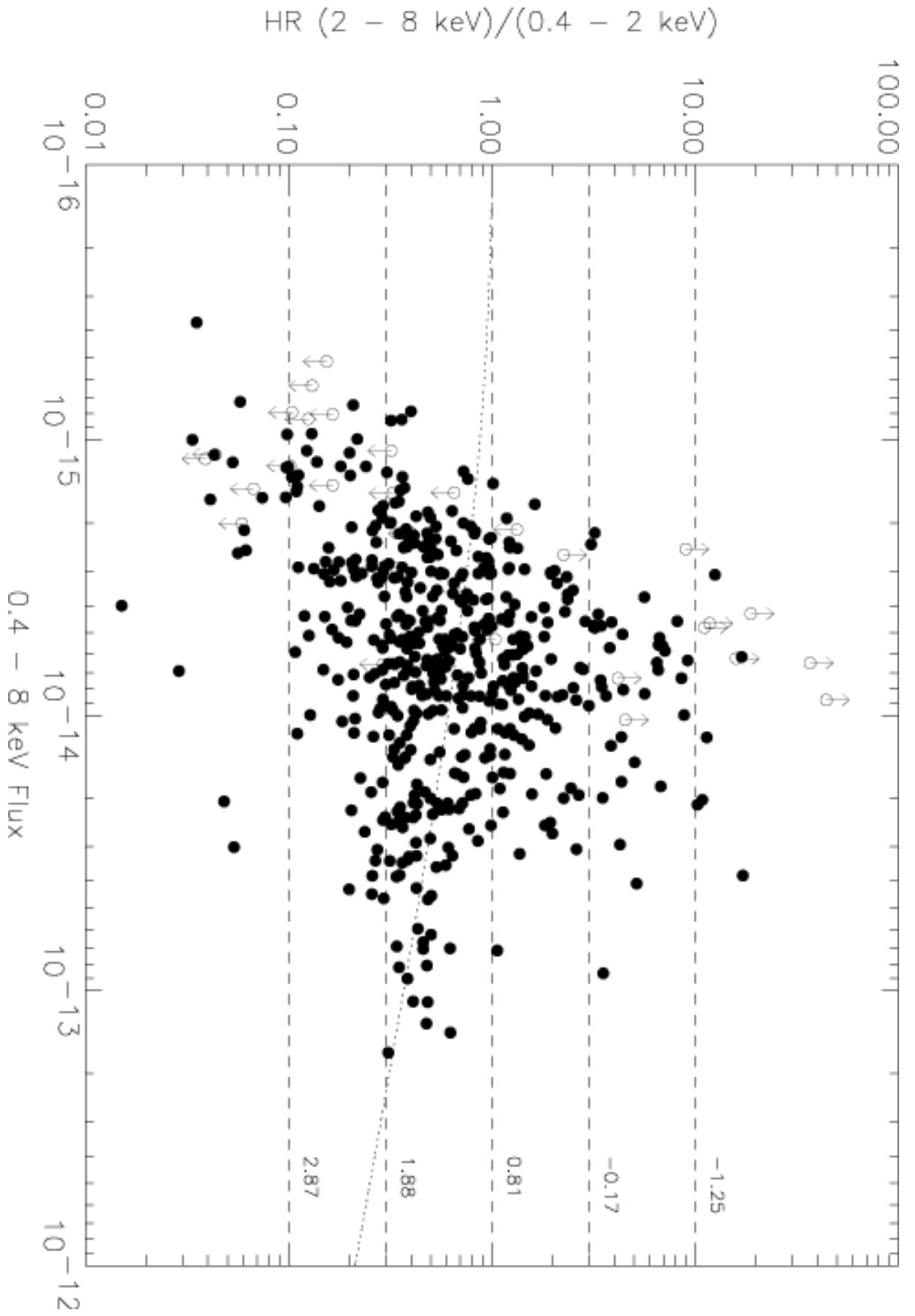


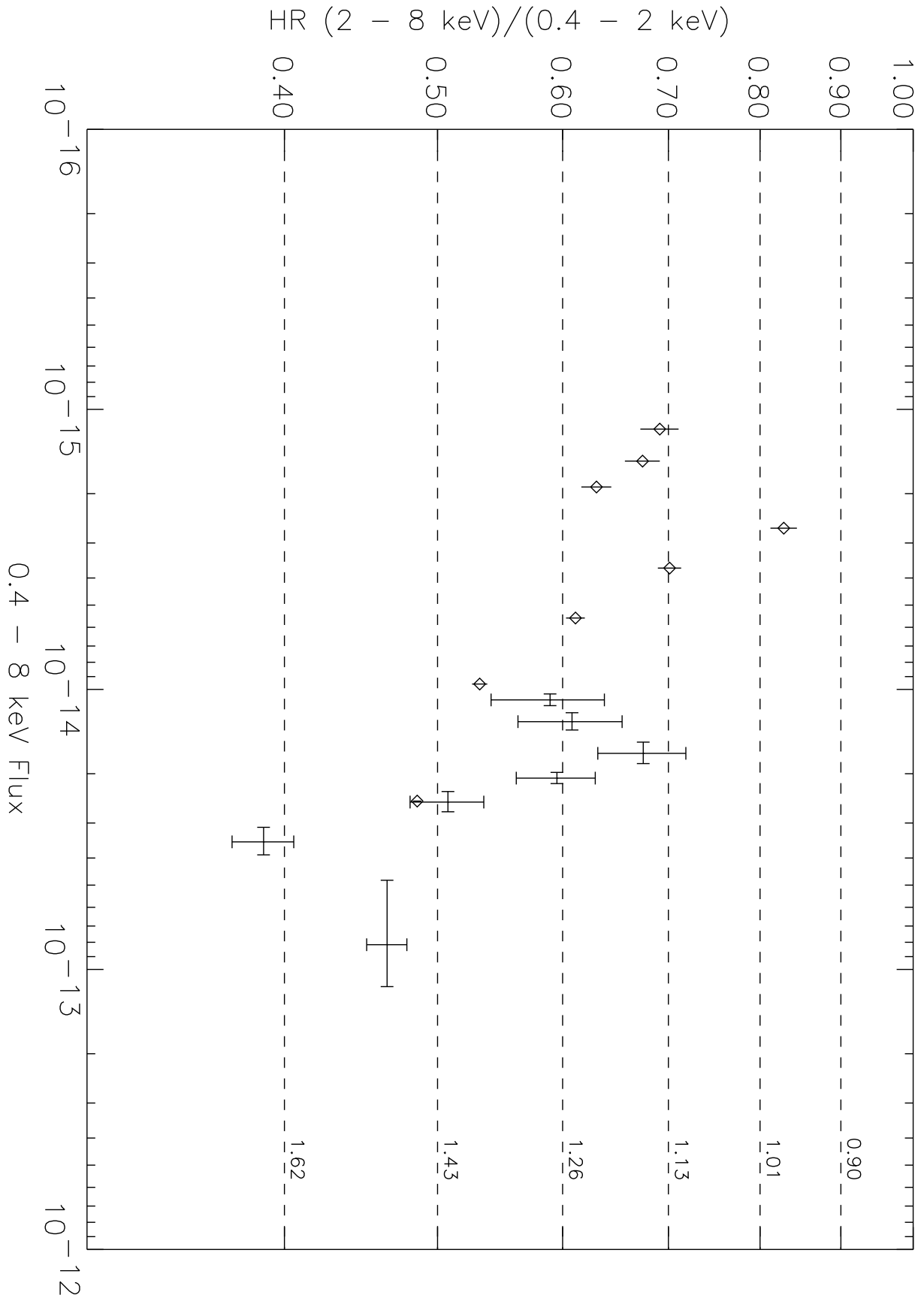




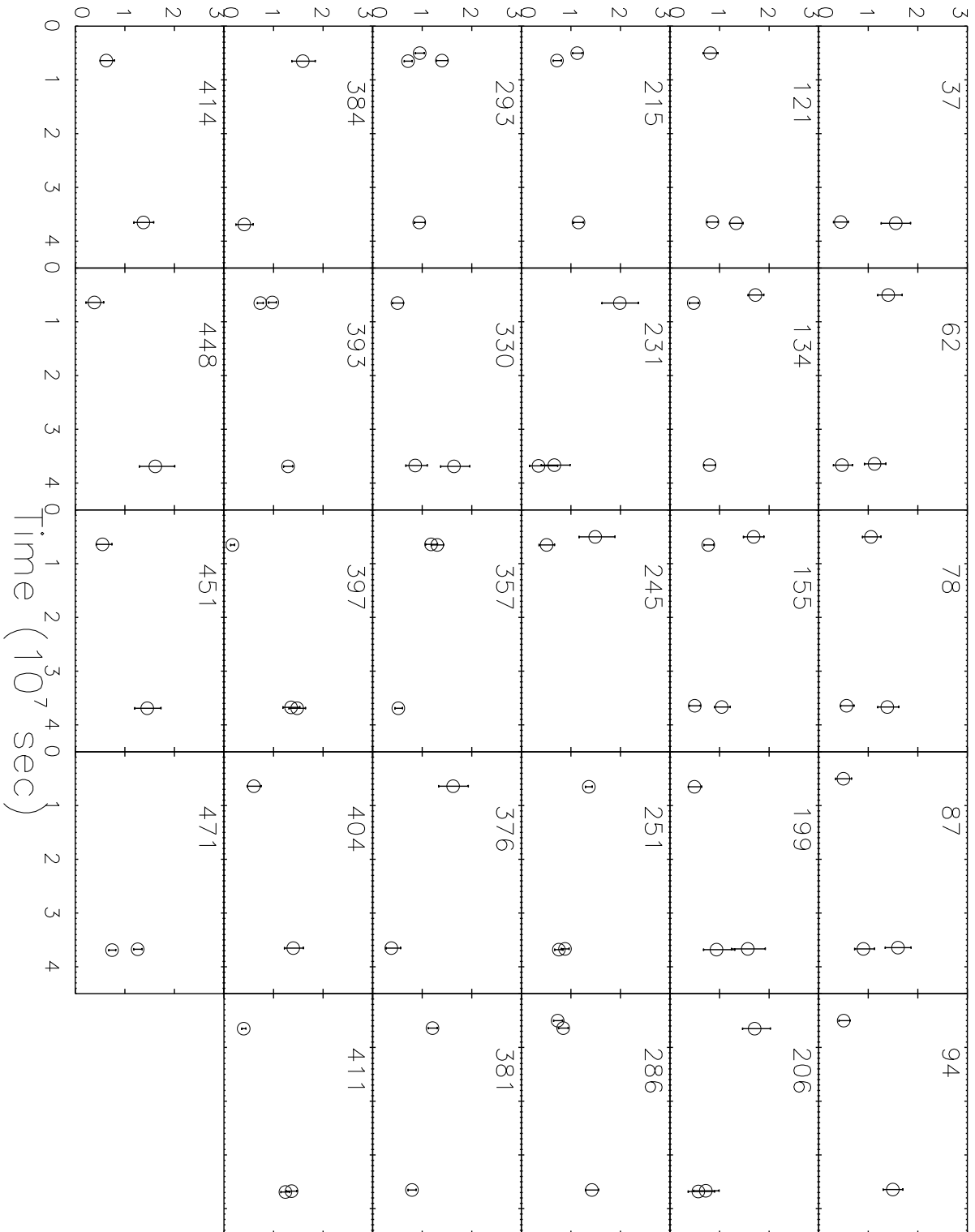


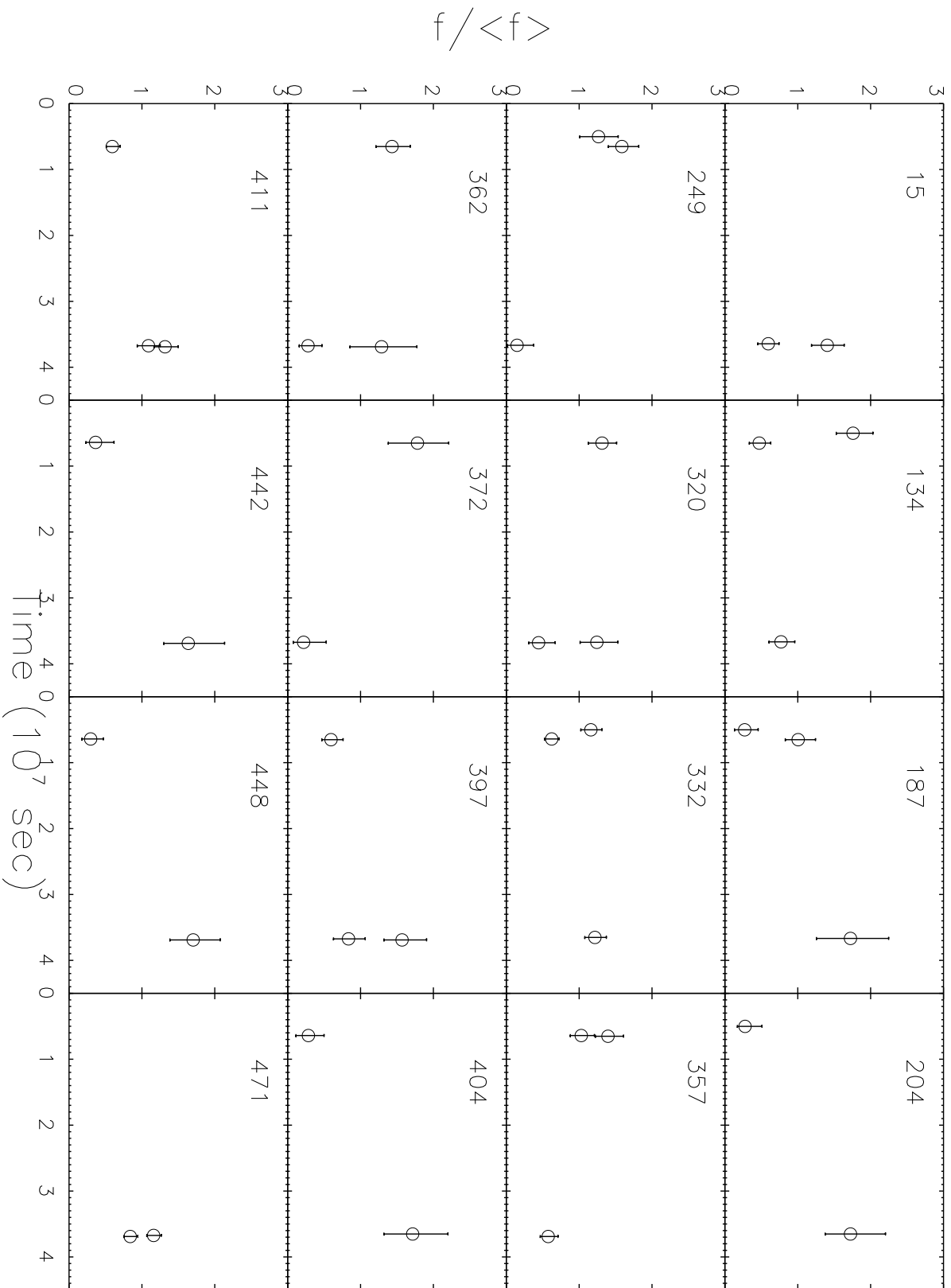


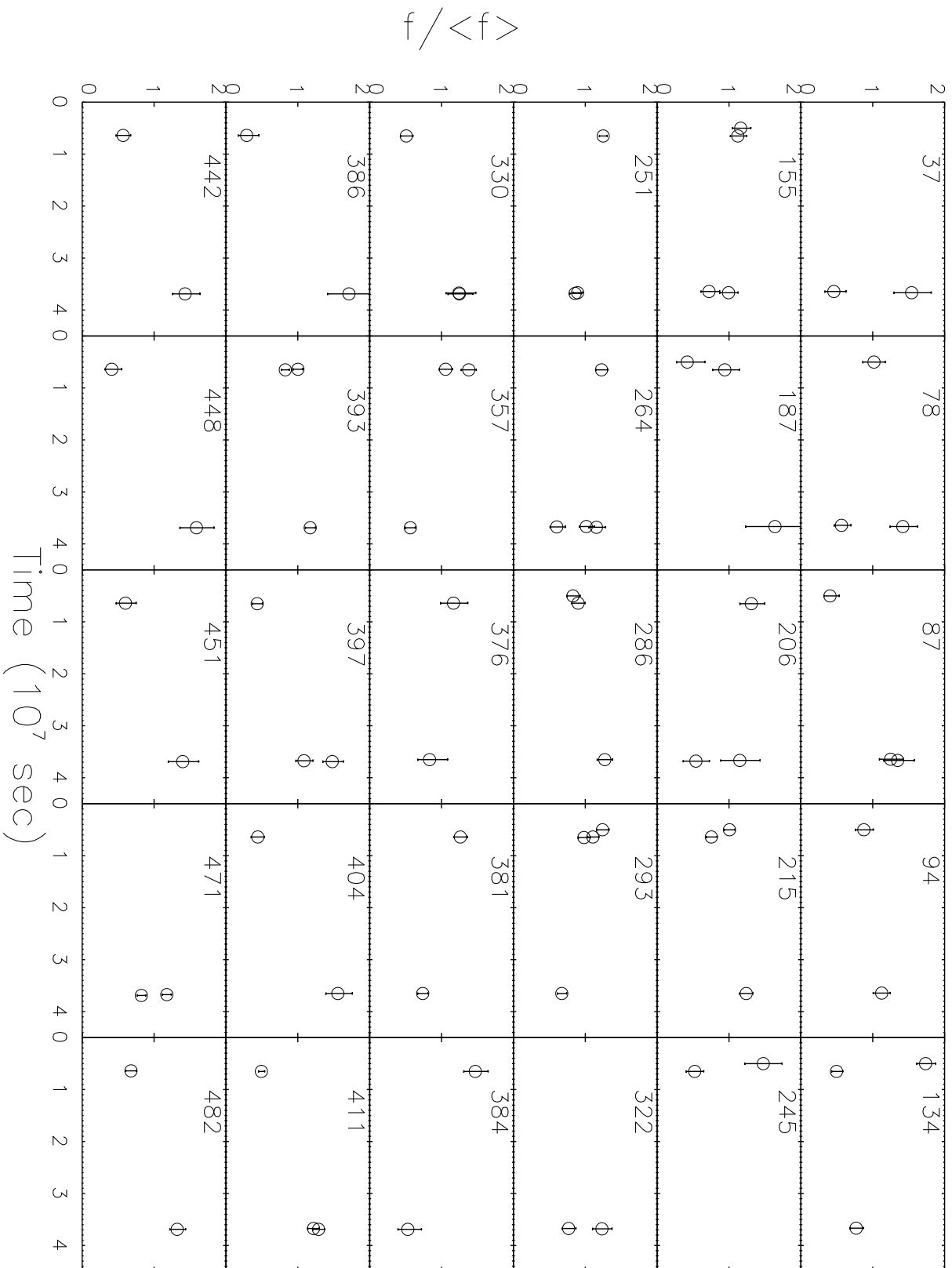


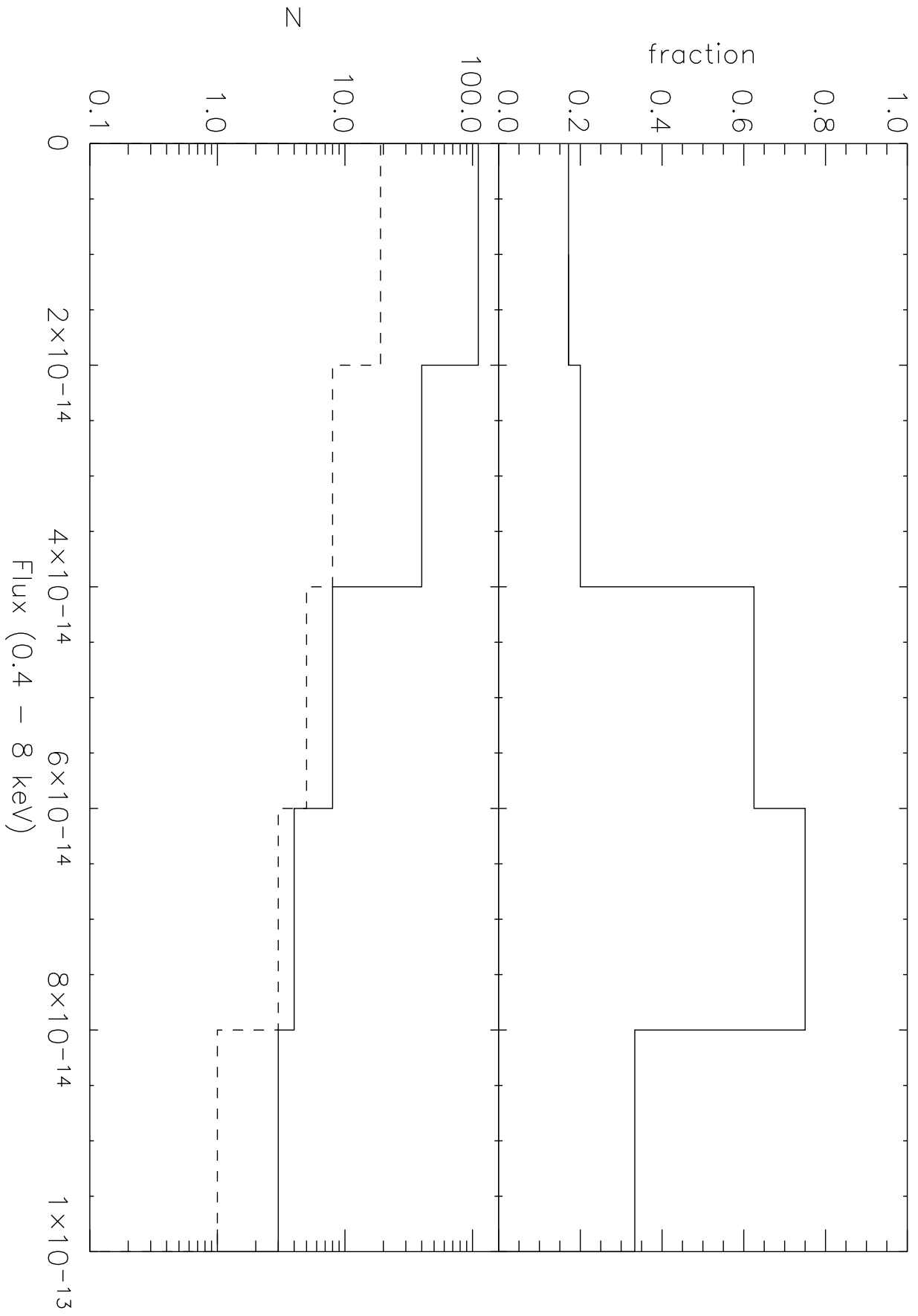


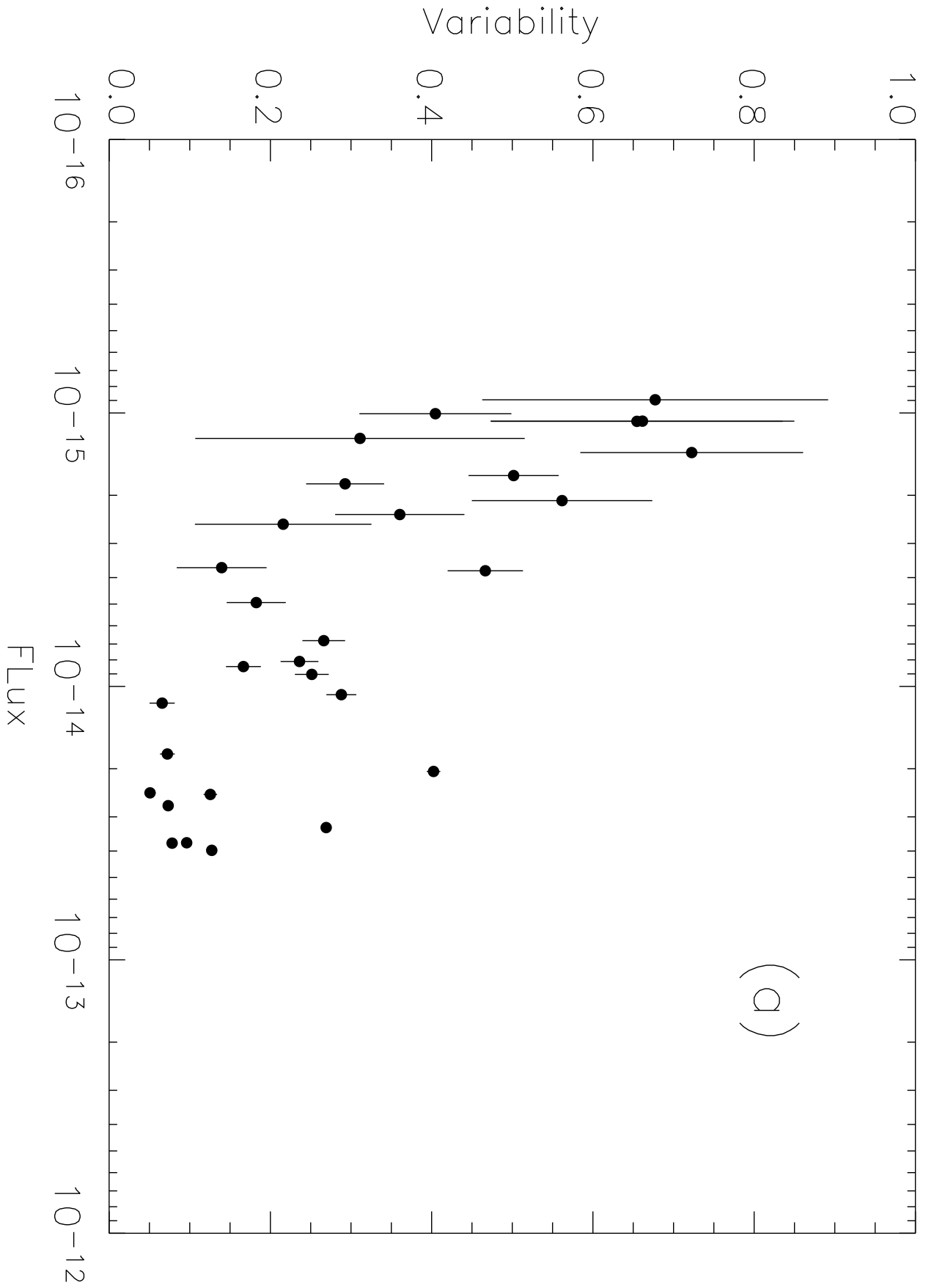
$f / \langle f \rangle$



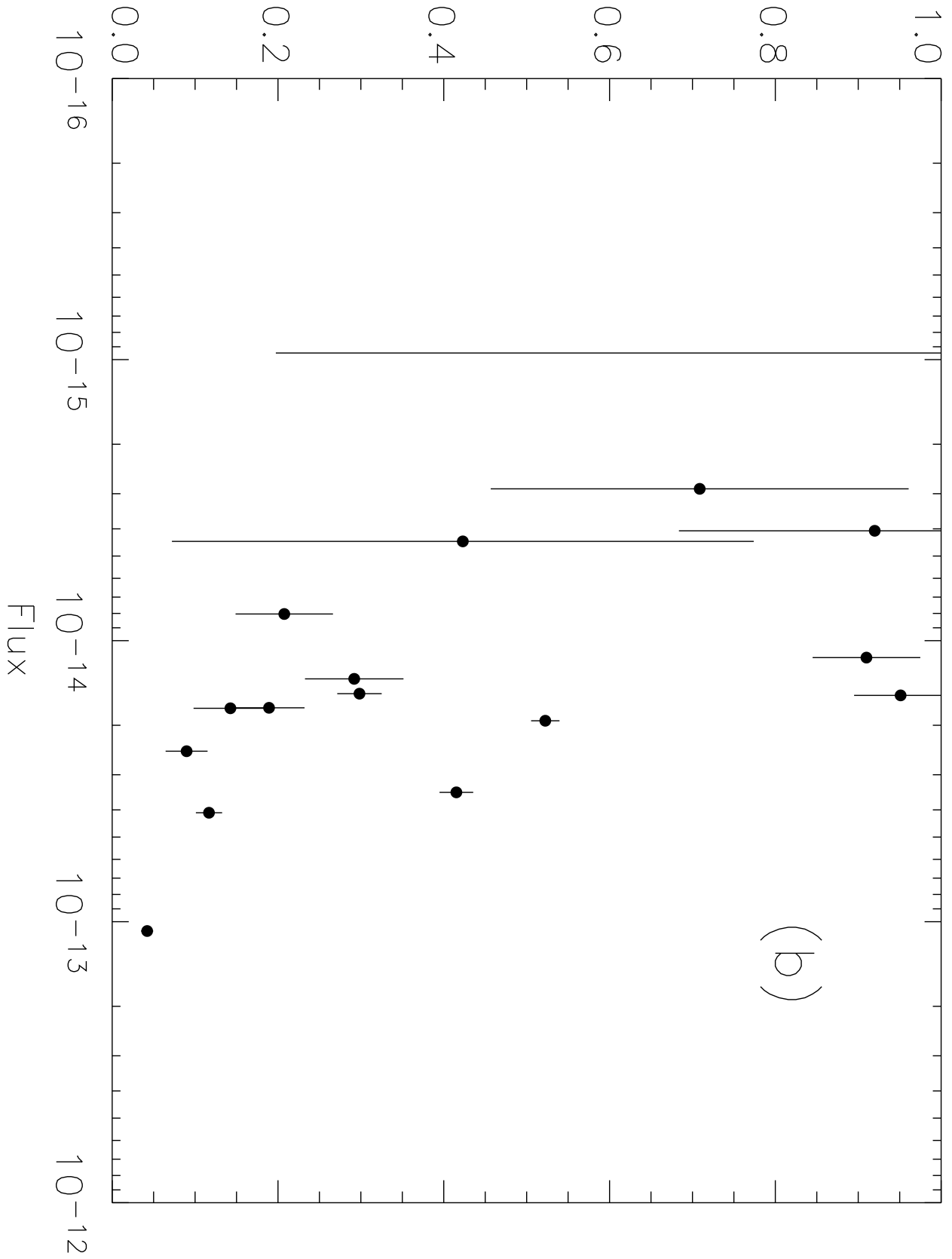








Variability



Variability

